nature

https://doi.org/10.1038/s41586-021-03631-y

Accelerated Article Preview

Diverse Functional Autoantibodies in Patients with COVID-19

Received: 4 December 2020

Accepted: 11 May 2021

Accelerated Article Preview Published online 19 May 2021

Cite this article as: Wang, E. Y. et al. Diverse Functional Autoantibodies in Patients with COVID-19. *Nature* https://doi.org/10.1038/s41586-021-03631-y (2021).

Eric Y. Wang, Tianyang Mao, Jon Klein, Yile Dai, John D. Huck, Jillian R. Jaycox, Feimei Liu, Ting Zhou, Benjamin Israelow, Patrick Wong, Andreas Coppi, Carolina Lucas, Julio Silva, Ji Eun Oh, Eric Song, Emily S. Perotti, Neil S. Zheng, Suzanne Fischer, Melissa Campbell, John B. Fournier, Anne L. Wyllie, Chantal B. F. Vogels, Isabel M. Ott, Chaney C. Kalinich, Mary E. Petrone, Anne E. Watkins, Yale IMPACT Team, Charles Dela Cruz, Shelli F. Farhadian, Wade L. Schulz, Shuangge Ma, Nathan D. Grubaugh, Albert I. Ko, Akiko Iwasaki & Aaron M. Ring

Article

Diverse Functional Autoantibodies in Patients with COVID-19

https://doi.org/10.1038/s41586-021-03631-y

Received: 4 December 2020

Accepted: 11 May 2021

Published online: 19 May 2021

Eric Y. Wang[1,16], Tianyang Mao[1,16], Jon Klein[1,16], Yile Dai[1,16], John D. Huck[1], Jillian R. Jaycox[1], Feimei Liu[1], Ting Zhou[1], Benjamin Israelow[1], Patrick Wong[1], Andreas Coppi[7], Carolina Lucas[1], Julio Silva[1], Ji Eun Oh[1], Eric Song[1], Emily S. Perotti[1], Neil S. Zheng[1], Suzanne Fischer[1], Melissa Campbell[5], John B. Fournier[5], Anne L. Wyllie[3], Chantal B. F. Vogels[3], Isabel M. Ott[3], Chaney C. Kalinich[3], Mary E. Petrone[3], Anne E. Watkins[3], Yale IMPACT Team*, Charles Dela Cruz[4], Shelli F. Farhadian[5], Wade L. Schulz[6,7], Shuangge Ma[8], Nathan D. Grubaugh[3], Albert I. Ko[3,5], Akiko Iwasaki[1,3,9]✉ & Aaron M. Ring[1,2]✉

COVID-19 manifests with a wide spectrum of clinical phenotypes that are characterized by exaggerated and misdirected host immune responses[1–6]. While pathological innate immune activation is well documented in severe disease[1], the impact of autoantibodies on disease progression is less defined. Here, we used a high-throughput autoantibody (AAb) discovery technique called Rapid Extracellular Antigen Profiling (REAP)[7] to screen a cohort of 194 SARS-CoV-2 infected COVID-19 patients and healthcare workers for autoantibodies against 2,770 extracellular and secreted proteins (the "exoproteome"). We found that COVID-19 patients exhibit dramatic increases in autoantibody reactivities compared to uninfected controls, with a high prevalence of autoantibodies against immunomodulatory proteins including cytokines, chemokines, complement components, and cell surface proteins. We established that these autoantibodies perturb immune function and impair virological control by inhibiting immunoreceptor signaling and by altering peripheral immune cell composition, and found that murine surrogates of these autoantibodies exacerbate disease severity in a mouse model of SARS-CoV-2 infection. Analysis of autoantibodies against tissue-associated antigens revealed associations with specific clinical characteristics and disease severity. In summary, these findings implicate a pathological role for exoproteome-directed autoantibodies in COVID-19 with diverse impacts on immune functionality and associations with clinical outcomes.

Humoral immunity plays dichotomous roles in COVID-19. Although neutralizing antibodies afford protection against SARS-CoV-2 infection[8,9], growing evidence suggests that dysregulated humoral immunity also contributes to the characteristic immunopathology of COVID-19[10–16]. Recent reports have identified isolated autoantibody reactivities in COVID-19 patients, including those that are characteristic of systemic autoimmune diseases[11–15]. Importantly, some autoantibodies, particularly neutralizing antibodies against IFN-I, appear to directly contribute to COVID-19 pathophysiology by antagonizing innate antiviral responses[11,12]. While striking examples of disease-modifying autoantibody responses have been described, the full breadth of autoantibody reactivities in COVID-19 and their immunological and clinical impacts remain undetermined.

A particularly important class of autoantibodies are those that target extracellular and secreted proteins (the "exoproteome"). Exoproteome-targeting autoantibodies can exert a wide range of functional effects. such as perturbation of cell signaling (as with the case of anti-IFN-I autoantibodies[11,12]) and targeted killing of specific cell populations via Fc receptors (FcR) and/or complement. We thus sought to identify functional autoantibody responses in COVID-19 patients by screening for autoantibody reactivities against the human exoproteome.

Widespread AAb elevation in COVID-19

To discover functional autoantibodies that could influence COVID-19 outcomes, we used a high-throughput autoantibody discovery method called Rapid Extracellular Antigen Profiling (REAP)[7]. REAP enables highly multiplexed detection of antibody reactivities through biopanning of patient IgG against a genetically-barcoded library of 2,770

[1]Department of Immunobiology, Yale School of Medicine, New Haven, CT, USA. [2]Department of Pharmacology, Yale School of Medicine, New Haven, CT, USA. [3]Department of Epidemiology of Microbial Diseases, Yale School of Public Health, New Haven, CT, USA. [4]Department of Medicine, Section of Pulmonary and Critical Care Medicine, Yale School of Medicine, New Haven, CT, USA. [5]Department of Internal Medicine (Infectious Diseases), Yale School of Medicine, New Haven, CT, USA. [6]Department of Laboratory Medicine, Yale School of Medicine, New Haven, CT, USA. [7]Center for Outcomes Research and Evaluation, Yale-New Haven Hospital, New Haven, CT, USA. [8]Department of Biostatistics, Yale School of Public Health, New Haven, CT, USA. [9]Howard Hughes Medical Institute, Chevy Chase, MD, USA. [16]These authors contributed equally: Eric Y. Wang, Tianyang Mao, Jon Klein, Yile Dai. *A list of authors and their affiliations appears at the end of the paper. ✉e-mail: akiko.iwasaki@yale.edu; aaron.ring@yale.edu

human extracellular proteins displayed on the surface of yeast, converting an antibody:antigen binding event into a quantitative sequencing readout ("REAP Score") based on the enrichment of each protein's barcodes (Extended Data Fig. 1a). To allow for detection of antibodies against coronavirus proteins, we additionally included the receptor binding domain (RBD) of SARS-CoV-2 and other common coronaviruses in the library (full antigen list in Supplementary Table 1).

We used REAP to screen samples from SARS-CoV-2 infected patients who were prospectively followed as part of the Yale Implementing Medical and Public Health Action Against Coronavirus CT (IMPACT) study (Extended Data Fig. 1b). This cohort includes 172 patients seen at Yale-New Haven Hospital with a range of clinical severities (as reported previously[1]) and 22 healthcare workers (HCWs) with mild illness or asymptomatic infection. Longitudinal samples were screened for a subset of the cohort. As uninfected controls, we screened 30 HCWs who tested negative for SARS-CoV-2 by RT-qPCR throughout their follow-up period in the IMPACT study. Patient demographics can be found in Extended Data Table 1. To validate the performance of REAP, we compared SARS-CoV-2 RBD REAP reactivity to that of ELISA (Extended Data Fig. 1c) and compared IL-6R REAP reactivity in patients who received anti-IL-6R therapeutic antibodies to those who did not (Extended Data Fig. 1d). We found strong concordance between REAP scores for SARS-CoV-2 RBD or IL-6R and SARS-CoV-2 RBD ELISA positivity or anti-IL-6R treatment respectively.

Next, we examined the total degree of autoreactivity in patients by quantifying the number of autoantibodies at different REAP score thresholds. Irrespective of the REAP score cutoff used, COVID-19 patients had a greater number of reactivities compared to controls, and the highest scoring reactivities were preferentially enriched in severe patients (Fig. 1a,b, Extended Data Fig. 2a). Of note, there was not a statistically significant difference in days from symptom onset (DFSO) between severe and moderate COVID-19 patients (Extended Data Fig. 2b), suggesting that the effects of temporal confounding were minimal. Given previously reported sex differences in the immune response to SARS-CoV-2[17], we compared the number of autoantibody reactivities between male and female patients and found no significant differences in reactivity numbers at any score cutoff (Extended Data Fig. 2c). Finally, compared to REAP profiles of SLE and autoimmune polyglandular syndrome type 1 (APS-1; APECED) patients, COVID-19 patients had greater numbers of reactivities compared to SLE, but fewer numbers of reactivities compared to APECED (Extended Data Fig. 2d). SLE and APECED patient demographics and clinical characteristics have been previously described[7]. Altogether, these results indicate that autoantibodies that target the exoproteome are elevated in COVID-19.

To investigate the temporal nature of these reactivities relative to COVID-19, we assessed longitudinal REAP score dynamics. Although definitive assignment was not possible due to lack of pre-infection samples, we inferred reactivities as "likely pre-existing", "newly acquired", or "waning" based on REAP score trajectories plotted against DFSO and anti-spike S1 IgG development. We found that some reactivities were present with high REAP scores within 10 DFSO and prior to the development of anti-spike S1 IgG responses, suggesting that they were likely pre-existing (Extended Data Fig. 3a,d). Others increased in score and tracked together with increasing anti-spike S1 IgG levels, indicating that they were newly acquired post-infection (Extended Data Fig. 3b,e). Finally, some reactivities decreased in REAP score over time while anti-spike S1 IgG increased or remained high, which suggests waning autoantibody titers (Extended Data Fig. 3c,f).

To further explore potential cellular sources of the elevated autoantibody reactivities in COVID-19 patients, we examined B cell phenotypes in peripheral blood mononuclear cells (PBMC) matching the REAP plasma samples. Similar to previous reports[10], we found that extrafollicular DN B cells are expanded in moderate and severe COVID-19 patients compared to uninfected controls (Extended Data Fig. 2f).

AAbs target immune-related proteins

Analysis of specific reactivities detected by REAP indicated that autoantibodies targeting immune-related proteins were elevated in severe COVID-19 patients (Fig. 1a,c, Extended Data Fig. 2e). These proteins included those involved in lymphocyte function/activation, leukocyte trafficking, type I and type III interferon responses, type II immunity, and the acute phase response. Confirming a recent report[11], we identified anti-IFN-I autoantibodies in 5.2% of hospitalized COVID-19 patients. Using ELISA, we orthogonally validated a subset of 22 autoantibodies that target cytokines, chemokines, growth factors, complement factors, and cell surface proteins (Extended Data Fig. 4a-d). These results demonstrate that COVID-19 patients possess autoantibodies that may affect a wide range of immunological functions.

To uncover the low-dimensional features in immune-targeting reactivities, we performed principal component analysis (PCA; Fig. 1d,e, Extended Data Fig. 4e). We found that the first principal component (PC1) was primarily composed of autoantibody reactivities against type I interferons (Fig. 1e) and separated a distinct cluster of samples with severe disease phenotype (Fig. 1d), consistent with Bastard et al.[11]. The next largest principal component (PC2) was composed of autoantibody reactivities against cytokines, chemokines, and the type III interferons, IFN-λ2 and IFN-λ3 (Fig. 1e). Notably, COVID-19 disease severity was a significant predictor of PC2 score (Extended Data Fig. 4f,g). Altogether, these findings suggest that autoantibodies against cytokines and chemokines may contribute to disease severity in COVID-19.

Virological/immunological AAb effects

Because autoantibodies in patients may influence circulating concentrations of their target proteins, we examined the plasma concentrations of cytokines and chemokines in patients with autoantibodies against these proteins. In some cases, autoantibodies were associated with apparent increases in their autoantigen targets (Extended Data Fig. 5b,f,j,m), whereas in other cases they correlated with apparent decreases (Extended Data Fig. 5k,l).

To more directly assess potential immunomodulatory effects of cytokine/chemokine targeting autoantibodies in COVID-19 patients, we assessed the *in vitro* activity of selected autoantibodies. We found that IgG from patients with anti-GM-CSF, anti-CXCL1, or anti-CXCL7 autoantibodies could antagonize signaling of GM-CSF, CXCL1, and CXCL7 respectively (Fig. 2a,b). In addition, we found that plasma or IgG from patients with anti-CD38 or anti-CD3ε autoantibodies led to increased macrophage antibody dependent cellular phagocytosis (ADCP) of Raji B cells or Jurkat T cells respectively (Fig. 2c, Extended Data Fig. 4h,i). Altogether, these results demonstrate that immune-targeting autoantibodies in COVID-19 patients can directly inhibit the activity of cytokines/chemokines and engage FcR effector functions that could lead to immune cell depletions in affected patients.

To investigate the potential virological effects of cytokine/chemokine targeting autoantibodies, we examined a subset of COVID-19 patients with anti-IFN-I autoantibodies. Consistent with prior reports[11], we found that these autoantibodies can neutralize IFN-I signaling activity *in vitro* (Extended Data Fig. 4j,k). To further assess their functional impacts, we compared longitudinal composite viral loads in patients who had anti-IFN-I autoantibodies to those who did not. After controlling for the contributions of age, sex, DFSO, and anti-SARS-CoV-2 IgG responses, patients with anti-IFN-I autoantibodies had significantly increased average viral loads relative to patients without anti-IFN-I autoantibodies (Fig. 2d, Extended Data Fig. 4l). We also found that patients with anti-IFN-I autoantibodies had extended hospital admission durations (Extended Data Fig. 4m). These results indicate that anti-IFN-I autoantibodies impair virological clearance in COVID-19 patients.

To investigate the *in vivo* effects of autoantibodies against immune cell surface proteins in COVID-19, we looked for associations between

these autoantibodies and blood leukocyte composition. First, we focused on two groups of antigens: those expressed on B cells (CD38, FcμR, FcRL3) and those preferentially expressed on classical/intermediate monocytes (CCR2, CCRL2, FFAR4, SYND4, CPAMD8; identified in a public RNA-seq dataset[18]). We found that patients with autoantibodies against B cell or classical/intermediate monocyte antigens had lower frequencies of B cells (Fig. 2e) and anti-SARS-CoV-2 RBD IgM (Extended Data Fig. 6a) or classical/intermediate monocytes (Fig. 2f, Extended Data Fig. 6b) respectively compared to autoantibody negative severity-matched patients. Looking at individual reactivities, we found that a patient with anti-CD3ε autoantibodies had intact B and NK cell compartments but dramatically reduced levels of $CD4^+$, $CD8^+$, and natural killer T cells (Fig. 2g, Extended Data Fig. 6c,d). Similarly, a patient with anti-CD38 autoantibodies exhibited a lower frequency of NK cells and activated $CD4^+$ or $CD8^+$ T cells, all of which also express CD38 (Extended Data Fig. 6f). Of note, we found that IgG or plasma from these patients could mediate ADCP against Jurkat or Raji cells respectively *in vitro* (Fig. 2c). In aggregate, these data show that autoantibodies targeting immune cell surface proteins may lead to depletion of specific immune cell populations in COVID-19 patients.

AAbs exacerbate disease severity in mice

To directly assess the impact of cytokine-targeting autoantibodies in COVID-19 pathogenesis *in vivo*, we used mice that transgenically express human ACE2 under the human keratin 18 promoter (K18-hACE2) in order to recapitulate aspects of human COVID-19 pathogenesis upon SARS-CoV-2 infection[19–21]. Given the enrichment of anti-IFN-I autoantibodies in severe COVID-19 patients, we first examined the impact of antibody-mediated IFN-I blockade *in vivo*. We found that mice pre-treated with neutralizing antibodies against the interferon-α/β receptor were more susceptible to SARS-CoV-2 infection; they had increased weight loss (Fig. 3a) and reduced survival (Fig. 3b). Additionally, compared to PBS-treated SARS-CoV-2 infected mice, anti-IFNAR treated infected mice exhibited impaired monocyte recruitment, maturation, and proinflammatory macrophage differentiation in the lungs (Extended Data Fig. 7b-d) as well as marked decreases in relative frequency and absolute number of activated ($CD44^+$,$CD69^+$) NK cells and $CD4^+$, $CD8^+$, and γδ T cells (Extended Data Fig. 7e,f). Collectively, these findings demonstrate that early blockade of IFN-I signaling by antibodies (which mimics the effects of pre-existing anti-IFN-I autoantibodies) results in exacerbated disease and interferes with myeloid/lymphoid activation in response to SARS-CoV-2 infection.

Beyond IFN-I, we identified COVID-19 patients with autoantibodies targeting components of the interleukin-18 (IL-18) pathway (IL-18Rβ in particular; Extended Data Fig. 4d), which plays a critical role in antiviral NK and $CD8^+$ T cell responses[22,23]. To examine the impact of IL-18 pathway disruption in SARS-CoV-2 infection, we administered neutralizing anti-IL-18 antibodies to K18-hACE2 mice immediately prior to infection. We found that IL-18 blockade greatly enhanced susceptibility to SARS-CoV-2 infection (Fig. 3d, Extended Data Fig. 7k), resulted in significantly higher viral burden (Extended Data Fig. 7g,h), and led to decreased frequency and number of effector NK cells with enhanced cytotoxic properties ($CD11b^+$ or $KLRG1^+$; Extended Data Fig. 7i,j). These results highlight the disruptive role that autoantibody-mediated IL-18 blockade can have in the immune response to SARS-CoV-2.

Furthermore, we identified IL-1β, IL-21, and GM-CSF as cytokine autoantibody targets in COVID-19 patients. IL-1β and IL-21 both participate directly in host antiviral defense[24,25], and IL-21 is a major contributor to PC2 in the PCA analysis of immune-targeting autoantibodies in COVID-19 (Fig. 1e). GM-CSF plays a critical role in augmenting alveolar macrophage-mediated innate antiviral defense[26]. Consistent with the antiviral properties of these three cytokines, we found that mice receiving anti-IL-1β, anti-IL-21R, or anti-GM-CSF antibodies became substantially more susceptible to SARS-CoV-2 infection as they had significantly decreased survival (Fig. 3e-g) and lost more weight (Extended Data Fig. 7l-n) upon SARS-CoV-2 infection compared to PBS-treated control mice.

Tissue-targeting AAb correlations

In addition to immune-targeting autoantibodies, we also observed a high prevalence of tissue-associated autoantibodies in COVID-19 patients (Fig. 4a). These autoantibodies were directed against vascular cells, coagulation factors and platelets, connective tissue, extracellular matrix components, and various organ systems including lung, the CNS compartment, skin, gastrointestinal tract, and other tissues. To assess whether any of these putative autoantigens were associated with significant perturbations in clinical phenotypes, we performed exploratory data analysis using a common, generalized linear mixed effects model (Extended Data Fig. 9). We found that certain autoantigens (*e.g.*, NXPH1, PCSK1, SLC2A10, and DCD) significantly correlated with clinical markers known to be associated with worsened COVID-19 disease severity (*e.g.*, D-dimer, ferritin, CRP, lactate)[27,28]. Given the extent of CNS-specific autoantigens identified in our REAP screen, and recent reports on the potential for SARS-CoV-2 neuroinvasion[29], we further examined whether any autoantibodies correlated with individual patient's Glasgow Coma Scale (GCS) scores. Intriguingly, we found that ten unique COVID-19 patients developed autoantibodies against HCRTR2, an orexin receptor enriched in the hypothalamus. We noted a marked negative correlation between levels of HCRTR2 autoantibodies in these patients and their exceptionally low GCS scores encompassing the time of sample collection (Fig. 4b). Furthermore, we validated the presence of these autoantibodies in two patients using an ELISA assay (Fig. 4c) and, using an *in vitro* orexin signaling assay, found that HCRTR2 autoantibodies in one patient were antagonized HCRTR2 activity (Fig. 4d).

Discussion

The surprising extent of autoantibody reactivities seen in patients with COVID-19 suggests humoral immunopathology is an intrinsic aspect of COVID-19 disease pathogenesis. Screening patient samples with the REAP platform, we identified and validated numerous protein targets across a wide range of tissues and immunological and physiological functions. These autoantibodies had potent functional activities and could be directly correlated with various virological, immunological, and clinical parameters *in vivo* within COVID-19 patient samples. Analysis of REAP score trajectories and comparisons to SARS-CoV-2 humoral responses suggest that some of these autoantibodies likely predated infection while others were induced following infection. Furthermore, murine surrogates of these autoantibodies led to increased disease severity in a mouse model of SARS-CoV-2 infection. Altogether, these results provide evidence that autoantibodies are capable of altering the course of COVID-19 by perturbing the immune response to SARS-CoV-2 and tissue homeostasis.

The diversity of autoantibody responses in COVID-19 patients also underscores the importance of high-throughput and unbiased proteome-scale surveys for autoantibody targets. Beyond validating the biologically-compelling example of anti-IFN-I antibodies in COVID-19, our studies implicated numerous other immune pathways targeted by autoantibodies in COVID-19 that were not previously associated with the disease. We also detected antibodies against various tissue-associated antigens and identified correlations between these antibodies and inflammatory clinical markers like D-dimer, ferritin, CRP, and lactate in COVID-19 patients. Intriguingly, many tissue autoantibodies we identified were also present across diverse physiological compartments frequently implicated during post-COVID syndrome (PCS)[30]. For example, we identified autoantibodies against the orexin receptor HCRTR2 that, *ex vivo*, could inhibit orexin signaling, which

plays an important role in regulating wakefulness and appetite[31]. Ultimately, whether the specific autoantibodies identified here play a role in the establishment of PCS, and whether they persist beyond the acute phase of COVID-19, warrants further investigation.

In summary, our analyses revealed an expansive autoantibody landscape in COVID-19 patients and identified distinct autoantibodies that exerted striking immunological and clinical outcomes. These results implicate previously underappreciated immunological pathways in the etiology of COVID-19 and suggest novel therapeutic paradigms centered around modulating these pathways, as well as attenuating the autoantibodies themselves. Finally, our findings provide a strong rationale for a wider investigation of autoantibodies in infectious disease pathogenesis.

Online content

Any methods, additional references, Nature Research reporting summaries, source data, extended data, supplementary information, acknowledgements, peer review information; details of author contributions and competing interests; and statements of data and code availability are available at https://doi.org/10.1038/s41586-021-03631-y.

1. Lucas, C. *et al*. Longitudinal analyses reveal immunological misfiring in severe COVID-19. *Nature* (2020) https://doi.org/10.1038/s41586-020-2588-y.
2. Maucourant, C. *et al*. Natural killer cell immunotypes related to COVID-19 disease severity. *Sci Immunol* **5**, (2020).
3. Mann, E. R. *et al*. Longitudinal immune profiling reveals key myeloid signatures associated with COVID-19. *Sci Immunol* **5**, (2020).
4. Lee, J. S. *et al*. Immunophenotyping of COVID-19 and influenza highlights the role of type I interferons in development of severe COVID-19. *Sci Immunol* **5**, (2020).
5. Rodrigues, T. S. *et al*. Inflammasomes are activated in response to SARS-CoV-2 infection and are associated with COVID-19 severity in patients. *J. Exp. Med*. **218**, (2021).
6. Vabret, N. *et al*. Immunology of COVID-19: Current State of the Science. *Immunity* **52**, 910–941 (2020).
7. Wang, E. Y. *et al*. REAP: A platform to identify autoantibodies that target the human exoproteome. *bioRxiv* (2021) https://doi.org/10.1101/2021.02.11.430703.
8. Hassan, A. O. *et al*. A SARS-CoV-2 Infection Model in Mice Demonstrates Protection by Neutralizing Antibodies. *Cell* **182**, 744–753.e4 (2020).
9. Garcia-Beltran, W. F. *et al*. COVID-19 neutralizing antibodies predict disease severity and survival. *Cell* **0**, (2020).
10. Woodruff, M. C. *et al*. Extrafollicular B cell responses correlate with neutralizing antibodies and morbidity in COVID-19. *Nat. Immunol*. 1–11 (2020).
11. Bastard, P. *et al*. Auto-antibodies against type I IFNs in patients with life-threatening COVID-19. *Science* (2020) https://doi.org/10.1126/science.abd4585.
12. Combes, A. J. *et al*. Global absence and targeting of protective immune states in severe COVID-19. *Nature* **591**, 124–130 (2021).
13. Zuo, Y. *et al*. Prothrombotic autoantibodies in serum from patients hospitalized with COVID-19. *Sci. Transl. Med*. **12**, (2020).
14. Woodruff, M. C., Ramonell, R. P., Lee, F. E.-H. & Sanz, I. Clinically identifiable autoreactivity is common in severe SARS-CoV-2 Infection. *Infectious Diseases (except HIV/AIDS)* 1400 (2020) https://doi.org/10.1101/2020.10.21.20216192.
15. Zhou, Y. *et al*. Clinical and Autoimmune Characteristics of Severe and Critical Cases of COVID-19. *Clin. Transl. Sci*. (2020) https://doi.org/10.1111/cts.12805.
16. Chang, S. E. *et al*. New-Onset IgG Autoantibodies in Hospitalized Patients with COVID-19. *medRxiv* (2021) https://doi.org/10.1101/2021.01.27.21250559.
17. Takahashi, T. *et al*. Sex differences in immune responses that underlie COVID-19 disease outcomes. *Nature* (2020) https://doi.org/10.1038/s41586-020-2700-3.
18. Monaco, G. *et al*. RNA-Seq Signatures Normalized by mRNA Abundance Allow Absolute Deconvolution of Human Immune Cell Types. *Cell Rep*. **26**, 1627–1640.e7 (2019).
19. McCray, P. B., Jr *et al*. Lethal infection of K18-hACE2 mice infected with severe acute respiratory syndrome coronavirus. *J. Virol.* **81**, 813–821 (2007).
20. Zheng, J. *et al*. COVID-19 treatments and pathogenesis including anosmia in K18-hACE2 mice. *Nature* **2020/11/10**, (2020).
21. Winkler, E. S. *et al*. SARS-CoV-2 infection of human ACE2-transgenic mice causes severe lung inflammation and impaired function. *Nat. Immunol*. **21**, 1327–1335 (2020).
22. Mantovani, A., Dinarello, C. A., Molgora, M. & Garlanda, C. Interleukin-1 and Related Cytokines in the Regulation of Inflammation and Immunity. *Immunity* **50**, 778–795 (2019).
23. Zhou, T. *et al*. IL-18BP is a secreted immune checkpoint and barrier to IL-18 immunotherapy. *Nature* **583**, 609–614 (2020).
24. Orzalli, M. H. *et al*. An Antiviral Branch of the IL-1 Signaling Pathway Restricts Immune-Evasive Virus Replication. *Mol. Cell* **71**, 825–840.e6 (2018).
25. Spolski, R. & Leonard, W. J. Interleukin-21: a double-edged sword with therapeutic potential. *Nat. Rev. Drug Discov*. **13**, 379–395 (2014).
26. Trapnell, B. C. & Whitsett, J. A. Gm-CSF regulates pulmonary surfactant homeostasis and alveolar macrophage-mediated innate host defense. *Annu. Rev. Physiol*. **64**, 775–802 (2002).
27. Wang, G. *et al*. C-Reactive Protein Level May Predict the Risk of COVID-19 Aggravation. *Open Forum Infect Dis* **7**, ofaa153 (2020).
28. Cheng, L. *et al*. Ferritin in the coronavirus disease 2019 (COVID-19): A systematic review and meta-analysis. *J. Clin. Lab. Anal*. **34**, e23618 (2020).
29. Song, E. *et al*. Neuroinvasion of SARS-CoV-2 in human and mouse brain. *J. Exp. Med*. **218**, (2021).
30. Nalbandian, A. *et al*. Post-acute COVID-19 syndrome. *Nat. Med*. **27**, 601–615 (2021).
31. Nixon, J. P. *et al*. Sleep disorders, obesity, and aging: the role of orexin. *Ageing Res. Rev*. **20**, 63–73 (2015).

Yale IMPACT Team

Abeer Obaid[10], Adam J. Moore[2], Arnau Casanovas-Massana[2], Alice Lu-Culligan[1], Allison Nelson[10], Angela Nunez[10], Anjelica Martin[1], Anne E. Watkins[2], Bertie Geng[10], Camila D. Odio[5], Christina A. Harden[2], Codruta Todeasa[10], Cole Jensen[2], Daniel Kim[1], David McDonald[10], Denise Shepard[10], Edward Courchaine[11], Elizabeth B. White[2], Erin Silva[10], Eriko Kudo[1], Giuseppe Deluliis[10], Harold Rahming[10], Hong-Jai Park[10], Irene Matos[10], Jessica Nouws[10], Jordan Valdez[10], Joseph Lim[12], Kadi-Ann Rose[10], Kelly Anastasio[13], Kristina Brower[2], Laura Glick[10], Lokesh Sharma[10], Lorenzo Sewanan[10], Lynda Knaggs[10], Maksym Minasyan[10], Maria Batsu[10], Maxine Kuang[2], Maura Nakahata[10], Melissa Linehan[1], Michael H. Askenase[14], Michael Simonov[10], Mikhail Smolgovsky[10], Nicole Sonnert[1], Nida Naushad[10], Pavithra Vijayakumar[10], Rick Martinello[3], Rupak Datta[3], Ryan Handoko[10], Santos Bermejo[10], Sarah Prophet[15], Sean Bickerton[11], Sofia Velazquez[14], Tyler Rice[1], William Khoury-Hanold[1], Xiaohua Peng[10], Yexin Yang[1], Yiyun Cao[1] & Yvette Strong[10]

[10]Yale School of Medicine, New Haven, CT, USA. [11]Department of Biochemistry and of Molecular Biology, Yale University School of Medicine, New Haven, CT, USA. [12]Yale Viral Hepatitis Program, Yale University School of Medicine, New Haven, CT, USA. [13]Yale Center for Clinical Investigation, Yale University School of Medicine, New Haven, CT, USA. [14]Department of Neurology, Yale University School of Medicine, New Haven, CT, USA. [15]Department of Molecular, Cellular and Developmental Biology, Yale University School of Medicine, New Haven, CT, USA.

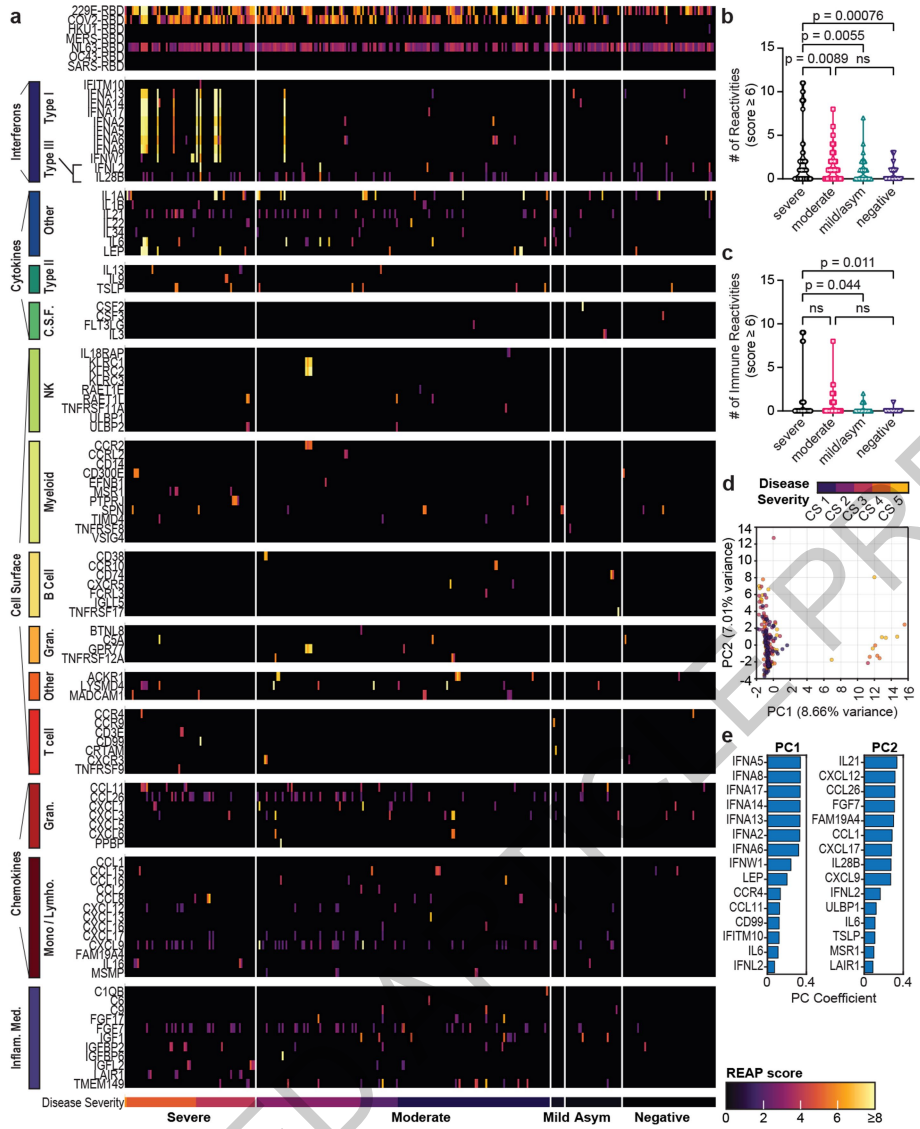

Fig. 1 | Immune-targeting autoantibodies are elevated in COVID-19 patients. a, Heatmap of immune-related protein REAP scores across all patient samples stratified by disease severity. **b,c**, Number of positive (REAP score ≥ 6) total reactivities (**b**) and immune-targeting reactivities (**c**) in severe disease (*n*=66), moderate disease (*n*=160), mild or asymptomatic disease (mild/asym.; *n*=36), and uninfected (negative; *n*=54) samples. Dashed lines indicate medians and dotted lines indicate first and third quartiles. **d**, Score plot of principal component analysis performed on immune-targeting reactivities in hospitalized COVID-19 patient samples (*n*=226) colored by clinical score (CS). **e**, Loadings for the first and second principal components from **d** in descending order. In **b-d**, *n* values include longitudinal samples from the same patient. Significance in **b,c** was determined using a linear mixed model with correction for multiple comparisons (see Methods).

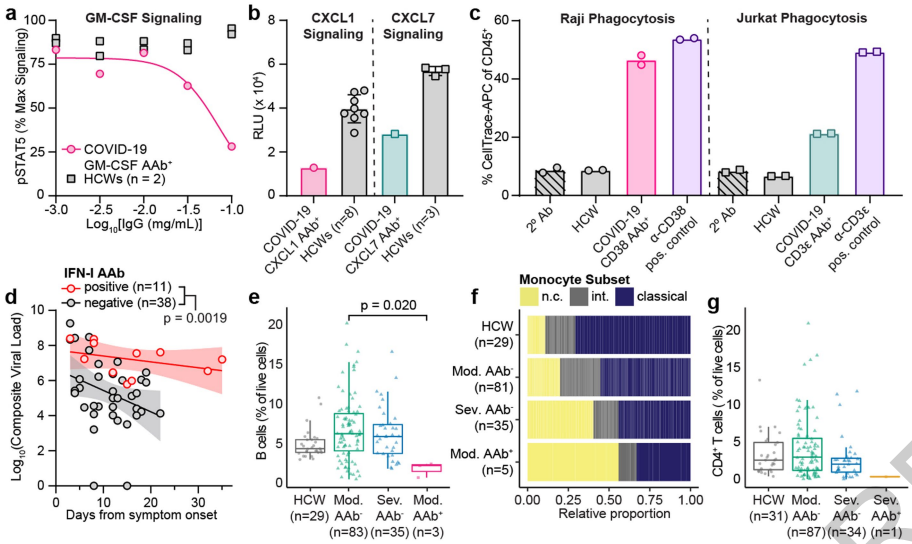

Fig. 2 | Immune-targeting autoantibodies in COVID-19 patients have functional effects. a, GM-CSF signaling assay performed with anti-GM-CSF autoantibody positive COVID-19 patient and uninfected healthcare worker (HCW) IgG. Results are averages of technical duplicates from one experiment. **b**, CXCL1 and CXCL7 signaling assays performed with anti-CXCL1 or anti-CXCL7 autoantibody positive COVID-19 patient and HCW IgG. Results are averages of 3 technical replicates or duplicates. **c**, Macrophage phagocytosis assay performed with Raji or Jurkat cells, anti-CD38 or anti-CD3ε autoantibody positive COVID-19 patient plasma or IgG respectively, anti-CD38 or anti-CD3ε monoclonal antibodies, and HCW plasma or IgG respectively (*n*=1 for all groups). Technical replicates are shown. Results in **b,c** are representative of two independent experiments. **d**, Longitudinal comparisons of SARS-CoV-2 viral load between patients with and without anti-IFN-I autoantibodies. Linear regressions (solid lines) and 95% confidence bands (shaded areas) for each group are displayed. *n* values include longitudinal samples from the same patient. **e-g**, Average percent B cells (**e**), relative proportions of classical, intermediate (int.), and nonclassical (n.c.) monocytes (**f**), and average percent CD4$^+$ T cells (**g**) among peripheral leukocytes in HCWs and COVID-19 patients stratified by disease severity and positive REAP reactivity (AAb$^+$; REAP score ≥ 2) against B cell displayed proteins (CD38, FcμR, FCRL3; **e**), proteins preferentially displayed on classical/intermediate monocyte (CCR2, CCRL2, FFAR4, SYND4, CPAMD8; **f**), and CD3ε (**g**) respectively. Data from **e,g** were presented as boxplots with the first quartile, median, third quartile, whiskers (minimum/maximum value within the first or third quartile ±1.5 times the interquartile range), and individual data points indicated. Significance was determined using a generalized linear mixed model (**d**; see Methods) or a two-sided Wilcoxon rank-sum test (**e**). In **b,c,e,f,g**, *n* values indicate samples from unique patients. All error bars represent standard deviation.

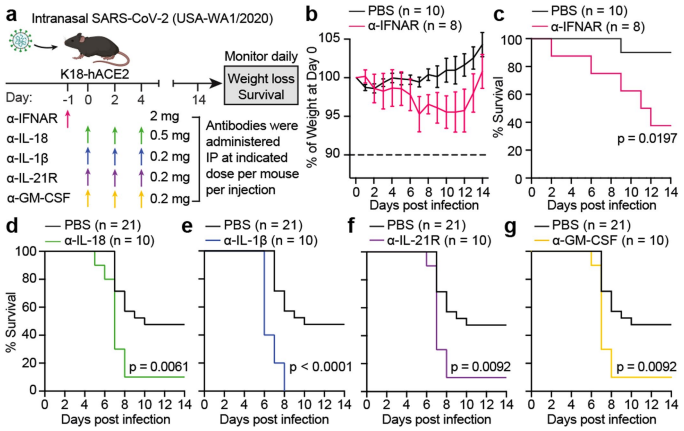

Fig. 3 | Immune-targeting autoantibodies exacerbate disease severity in a COVID-19 mouse model. a, K18-hACE2 mice were intranasally infected with sublethal dose (**b,c**) or median lethal dose (**d-g**) SARS-CoV-2 (USA-WA1/2020 isolate) and treated with indicated antibodies. **b-c**, Normalized body weight (**b**) and survival defined as 10% weight loss or mortality (**c**) of PBS or α-IFNAR-treated mice from day 1 to 14 post infection. **d-g**, Survival defined as 20% weight loss or mortality of α-IL-18 (**d**), α-IL-1β (**e**), α-IL-21R (**f**), α-GM-CSF (**g**), and PBS-treated K18 mice from day 1 to 14 post infection. Significance in **c-g** was determined using log-rank (Mantel-Cox) test. All error bars in this figure represent standard error of the mean. All *n* values indicate biologically independent animals examined over 2 independent experiments.

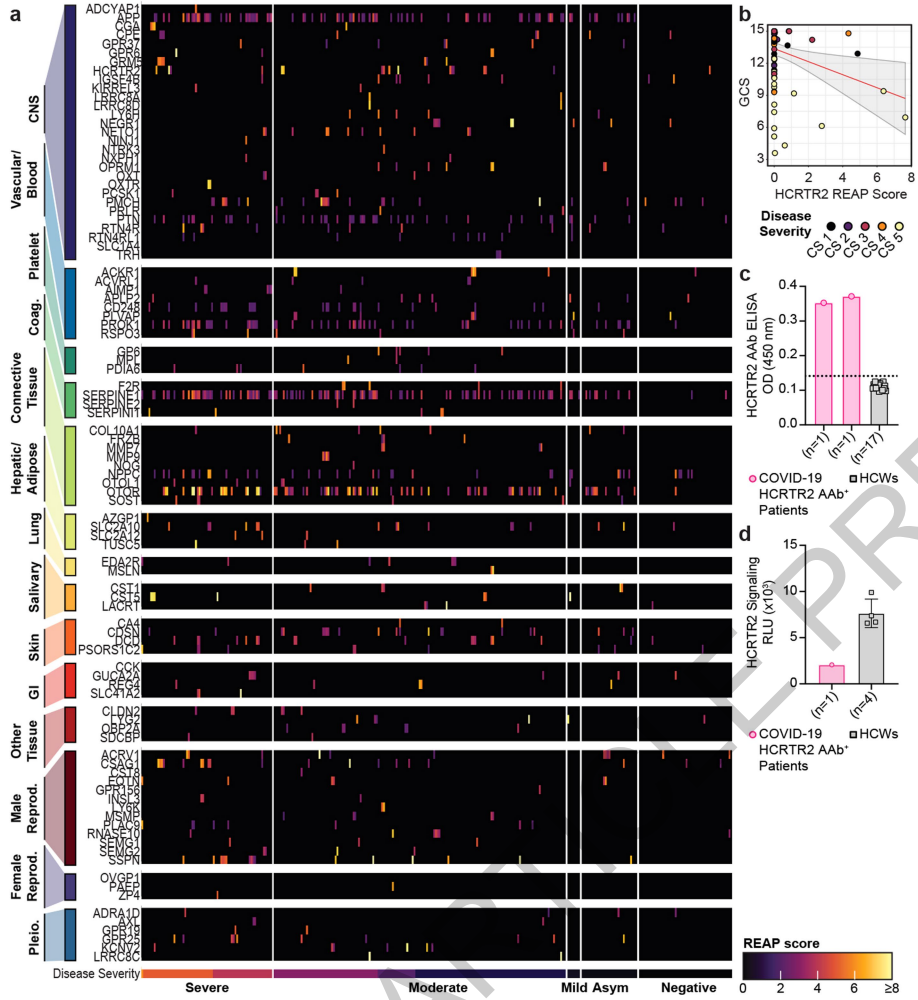

Fig. 4 | Autoantibodies against tissue-associated antigens are prevalent and functional in COVID-19 patients. a, Heatmap of tissue-associated REAP scores stratified by disease severity. **b**, Correlation of HCRTR2 REAP scores with Glasgow Coma Scale scores in COVID-19 patients (n=89, Spearman's ρ=-0.20, p=0.052). Linear regression (solid lines) and 95% confidence bands (shaded areas) are displayed. Patients are colored by clinical score (CS). Significance of Spearman's correlation was determined via asymptotic t approximation with a two-sided test. **c**, Single point pan-IgG HCRTR2 autoantibody ELISA conducted with 1:50 plasma dilution. Dotted line represents the uninfected control (HCW) average plus 3 standard deviations. Results are averages of technical duplicates from one experiment. **d**, Orexin signaling assay performed with anti-HCRTR2 autoantibody positive COVID-19 patient and HCW IgG. Results are averages of 3 technical replicates from one experiment. All n values indicate samples from unique patients. All error bars represent standard deviation.

Methods

Ethics statement

This study was approved by Yale Human Research Protection Program Institutional Review Boards (FWA00002571, protocol ID 2000027690). Informed consent was obtained from all enrolled patients and healthcare workers.

Patients

As previously described[1] and reproduced here for accessibility, 197 patients admitted to YNHH with COVID-19 between 18 March 2020 and 5 May 2020 were included in this study. No statistical methods were used to predetermine sample size. Nasopharyngeal and saliva samples were collected as described[32], approximately every four days, for SARS-CoV-2 RT–qPCR analysis where clinically feasible. Paired whole blood for flow cytometry analysis was collected simultaneously in sodium heparin-coated vacutainers and kept on gentle agitation until processing. All blood was processed on the day of collection. Patients were scored for COVID-19 disease severity through review of electronic medical records (EMR) at each longitudinal time point. Scores were assigned by a clinical infectious disease physician according to a custom-developed disease severity scale. Moderate disease status (clinical score 1–3) was defined as: SARS-CoV-2 infection requiring hospitalization without supplementary oxygen (1); infection requiring non-invasive supplementary oxygen (<3 l/min to maintain SpO_2 >92%) (2); and infection requiring non-invasive supplementary oxygen (>3 l/min to maintain SpO_2 >92%, or >2 l/min to maintain SpO_2 >92% and had a high-sensitivity C-reactive protein (CRP) >70) and received tocilizumab). Severe disease status (clinical score 4 or 5) was defined as infection meeting all criteria for clinical score 3 and also requiring admission to the ICU and >6 l/min supplementary oxygen to maintain SpO_2 >92% (4); or infection requiring invasive mechanical ventilation or extracorporeal membrane oxygenation (ECMO) in addition to glucocorticoid or vasopressor administration (5). Clinical score 6 was assigned for deceased patients. For all patients, days from symptom onset were estimated as follows: (1) highest priority was given to explicit onset dates provided by patients; (2) next highest priority was given to the earliest reported symptom by a patient; and (3) in the absence of direct information regarding symptom onset, we estimated a date through manual assessment of the electronic medical record (EMRs) by an independent clinician. Demographic information was aggregated through a systematic and retrospective review of patient EMRs and was used to construct Extended Data Table 1. The clinical data were collected using EPIC EHR and REDCap 9.3.6 software. At the time of sample acquisition and processing, investigators were unaware of the patients' conditions. Blood acquisition was performed and recorded by a separate team. Information about patients' conditions was not available until after processing and analysis of raw data by flow cytometry and ELISA. A clinical team, separate from the experimental team, performed chart reviews to determine relevant statistics. Cytokines and FACS analyses were performed blinded. Patients' clinical information and clinical score coding were revealed only after data collection.

Clinical data acquisition

Clinical data for patients and healthcare workers were extracted from the Yale-New Haven Health computational health platform[33,34] in the Observational Medical Outcomes Partnership (OMOP) data model. For each research specimen, summary statistics including minimum, mean, median, and maximum values were obtained for relevant clinical measurements, including the Glasgow Coma Scale, within ±1 day from the time of biospecimen collection. Disease severity endpoints, including admission, supplemental oxygen use, and invasive ventilation were validated as previously described[35].

Yeast induction

All yeast were induced as previously described[7]. In short, one day prior to induction, yeast were expanded in synthetic dextrose medium lacking uracil (SDO -Ura) at 30 °C. The following day, yeast were induced by resuspension at an optical density of 1 in synthetic galactose medium lacking uracil (SGO -Ura) supplemented with 10% SDO - Ura and culturing at 30 °C for approximately 18 hours.

Rapid Extracellular Antigen Profiling (REAP)

IgG antibody isolation for REAP was performed as previously described[7]. In short, Triton X-100 and RNase A were added to plasma samples at final concentrations of 0.5% and 0.5 mg mL^{-1} respectively and incubated at room temperature for 30 min before use to reduce risk from any potential virus in plasma. 20 µL protein G magnetic resin (Lytic Solutions) was washed with sterile PBS, resuspended in 75 µL sterile PBS, and added to 25 µL plasma. plasma-resin mixture was incubated overnight at 4 °C with shaking. Resin was washed with sterile PBS, resuspended in 90 µL 100 mM glycine pH 2.7, and incubated for five min at RT. Supernatant was extracted and added to 10 µL sterile 1M Tris pH 8.0. At this point, IgG concentration was measured using a NanoDrop 8000 Spectrophotometer (Thermo Fisher Scientific). To generate yeast-depleted IgG for use in REAP, purified IgG was added to 10^8 induced empty vector (pDD003) yeast and incubated for 3 hours at 4 °C with shaking. Yeast-IgG mixtures were placed into 96 well 0.45 um filter plates (Thomas Scientific) and yeast-depleted IgG was eluted into sterile 96 well plates by centrifugation at 3000 g for 3 min.

Yeast library selection for REAP was performed as previously described[7]. In short, 400 µL of the induced yeast library was set aside to allow for comparison to post-selection libraries. 10^8 induced yeast were added to wells of a sterile 96-well v-bottom microtiter plate, resuspended in 100 µL PBE (PBS with 0.5% BSA and 0.5 mM EDTA) containing 10 µg patient-derived antibody, and incubated with shaking for 1 hour at 4 °C. Yeast were washed twice with PBE, resuspended in 100 µL PBE with a 1:100 dilution of biotin anti-human IgG Fc antibody (clone HP6017, BioLegend), and incubated with shaking for 1 hour at 4 °C. Yeast were washed twice with PBE, resuspended in 100 µL PBE with a 1:20 dilution of Streptavidin MicroBeads (Miltenyi Biotec), and incubated with shaking for 30 min at 4 °C. All following steps were carried out at RT. Multi-96 Columns (Miltenyi Biotec) were placed into a MultiMACS M96 Separator (Miltenyi Biotec) in positive selection mode and the columns were equilibrated with 70% ethanol and degassed PBE. Yeast were resuspended in 200 µL degassed PBE and placed into the columns. The columns were washed three times with degassed PBE. To elute the selected yeast, columns were removed from the separator and placed over 96-well deep well plates. 700 µL degassed PBE was added to each well of the column and the column and deep well plate were centrifuged briefly. This process was repeated 3 times. Yeast were recovered in 1 mL SDO -Ura at 30 °C.

DNA was extracted from yeast libraries using Zymoprep-96 Yeast Plasmid Miniprep kits or Zymoprep Yeast Plasmid Miniprep II kits (Zymo Research) according to standard manufacturer protocols. A first round of PCR was used to amplify a DNA sequence containing the protein display barcode on the yeast plasmid. PCR reactions were conducted using 1 µL plasmid DNA, 159_DIF2 and 159_DIR2 primers, and the following PCR settings: 98 °C denaturation, 58 °C annealing, 72 °C extension, 25 rounds of amplification. A second round of PCR was conducted using 1 µL first round PCR product, Nextera i5 and i7 dual-index library primers (Illumina) along with dual-index primers containing custom indices, and the following PCR settings: 98 °C denaturation, 58 °C annealing, 72 °C extension, 25 rounds of amplification. PCR products were pooled and run on a 1% agarose gel. The band corresponding to 257 base pairs was cut out and DNA (NGS library) was extracted using a QIAquick Gel Extraction Kit (Qiagen) according to standard manufacturer protocols. NGS library was sequenced using

an Illumina NextSeq 500 and NextSeq 500/550 75 cycle High Output Kit v2.5 with 75 base pair single-end sequencing according to standard manufacturer protocols. A minimum of 50,000 reads per sample was collected and the pre-selection library was sampled at ten times greater depth than other samples.

REAP data analysis

REAP score was calculated as previously described[7] and reproduced here. First, barcode counts were extracted from raw NGS data using custom codes. Next, aggregate and clonal enrichment was calculated using edgeR[36] and custom codes. For aggregate enrichment, barcode counts across all unique barcodes associated with a given protein were summed, library sizes across samples were normalized using default edgeR parameters, common and tagwise dispersion were estimated using default edgeR parameters, and exact tests comparing each sample to the pre-selection library were performed using default edgeR parameters. Aggregate enrichment is thus the $\log_2$ fold change values from these exact tests with zeroes in the place of negative fold changes. Log_2 fold change values for clonal enrichment were calculated in an identical manner, but barcode counts across all unique barcodes associated with a given protein were not summed. Clonal enrichment for a given reactivity was defined as the fraction of clones out of total clones that were enriched ($\log_2$ fold change ≥ 2). Thus, the clonal enrichment metric progressively penalizes proteins with lower fractions of clones enriched. This metric was implemented because a true reactivity should theoretically enrich all yeast clones displaying a given protein.

Aggregate (E_a) and clonal enrichment (E_c) for a given protein, a scaling factor (β_u) based on the number of unique yeast clones (yeast that have a unique DNA barcode) displaying a given protein, and a scaling factor (β_f) based on the overall frequency of yeast in the library displaying a given protein were used as inputs to calculate the REAP score, which is defined as follows.

$$\text{REAP score} = E_a \times (E_c)^2 \times \beta_u \times \beta_f$$

β_u and β_f are logarithmic scaling factors that progressively penalize the REAP score of proteins with low numbers of unique barcodes or low frequencies in the library. β_u is applied to proteins with ≤ 5 unique yeast clones in the library and β_f is applied to proteins with a frequency ≤ 0.0001 in the library. β_f was implemented to mitigate spurious enrichment signals from low frequency proteins, which could occur due to sequencing errors or stochasticity in the selection process. β_u was implemented because the clonal enrichment metric is less valid for proteins with low numbers of unique yeast clones, decreasing confidence in the validity of the reactivity. β_u and β_f are defined as follows where x_u is the number of unique yeast clones for a given protein and x_f is the $\log_{10}$ transformed frequency of a given protein in the library.

$$\beta_u = \ln(x_u + 0.5)/1.705$$

$$\beta_f = \ln(x_f + 7.1)/1.16$$

Antigens (excluding coronavirus RBDs and IL6R) with an average REAP score greater than 0.5 across all samples were defined as "sticky" and excluded from further analysis. Antigens defined as immune-targeting and tissue-associated were manually identified.

Autoantibody enzyme-linked immunosorbent assay (ELISA) measurement

200 ng of purchased or independently produced recombinant protein in 100 µL of PBS pH 7.0 was added to 96-well flat-bottom Immulon 2HB plates (Thermo Fisher Scientific) and placed at 4 °C overnight. Plates were washed once with 225 µL ELISA wash buffer (PBS + 0.05% Tween 20) and 150 µL ELISA blocking buffer (PBS + 2% Human Serum Albumin) was added to the well. Plates were incubated for 2 hours at RT. ELISA blocking buffer was removed from the wells and appropriate dilutions of sample plasma in 100 µL ELISA blocking buffer were added to each well. Plates were incubated for 2 hours at RT. Plates were washed 6 times with 225 µL ELISA wash buffer and 1:5000 goat anti-human IgG HRP (Millipore Sigma) or anti-human IgG isotype-specific HRP (Southern Biotech; IgG1: clone HP6001, IgG2: clone 31-7-4, IgG3: clone HP6050, IgG4: clone HP6025) in 100 µL ELISA blocking buffer was added to the wells. Plates were incubated for 1 hour at RT. Plates were washed 6 times with 225 µL ELISA wash buffer. 50 µL TMB substrate (BD Biosciences) was added to the wells and plates were incubated for 20-30 min in the dark at RT. 50 µL 1 M sulfuric acid was added to the wells and absorbance at 450 nm was measured in a Synergy HTX Multi-Mode Microplate Reader (BioTek). Proteins used are as follows: ACKR1-mIgG2a-Fc (produced in-house), BAMBI (Sino Biological, 10890-H08H-20), C1qB (Sino Biological, 10941-H08B-20), CCL15 (PeproTech, 300-43), CCL16 (PeproTech, 300-44), CNPY3 (produced in-house), CNPY4 (produced in-house), CST5 (produced in-house), CD38 (R&D Systems, 2404-AC-010), GM-CSF (produced in-house), CXCL1 (PeproTech, 300-11), CXCL3 (PeproTech, 300-40), CXCL7 (PeproTech, 300-14), FcµR (R&D Systems, 9494-MU-050), HCRTR2-mIgG2a-Fc (produced in-house), IFN-ω (PeproTech, 300-02J), IL-13 (PeproTech, 200-13), IL-1α (RayBiotech, 228-10846-1), IL-6 (produced in-house), Leptin (R&D Systems, 398-LP-01M), SLC2A12-mIgG2a-Fc (produced in-house), TSLP (PeproTech, 300-62), IL-18Rβ (produced in-house).

Functional validation of anti-GM-CSF and anti-IFN-I autoantibodies

TF-1 cells (ATCC, CRL-2003) were cultured in RPMI (+ 10% heat inactivated FBS, 10 U/mL Penicillin, 100 mg/mL Streptomycin, 1 mM sodium pyruvate, 2 ng/mL GM-CSF (PeproTech, 300-03)) and incubated at 37 °C, 5% CO_2. THP-1 cells (ATCC, TIB-202) were cultured in RPMI (+ 10% heat inactivated FBS, 10 U/mL Penicillin, 100 mg/mL Streptomycin) and incubated at 37 °C, 5% CO_2. For validation of GM-CSF autoantibodies, TF-1 cells were starved of recombinant GM-CSF eighteen hours prior to experiments. GM-CSF at 200 pg/mL was incubated with dilutions of purified IgG for 15 min at room temperature and then used to stimulate TF-1 cells in a 96-well plate (2×10^5 cells per well) in a final volume of 100 µL (final concentration of 100 pg/mL). For validation of IFN autoantibodies, IFNα2 (R&D Systems, 11100-1) and IFNω (Peprotech, 300-02J) at 1500 pg/mL and 2000 pg/mL, respectively, were incubated with dilutions of purified IgG for 15 min at room temperature and then used to stimulate THP-1 cells in a 96-well plate (3.5 x 105 cells per well) in a final volume of 100 µL (final concentrations of 750 and 1000 pg/mL, respectively). IgG was purified from plasma using protein G magnetic beads (Lytic Solutions) as previously described[7]. After 15 min of stimulation, cells were fixed in 4% paraformaldehyde for 30 mins, washed with PBS, and permeabilized in 100% methanol on ice for 45 minutes. Cells were then washed twice with PBE and stained with PE conjugated anti-STAT5 pY694 (1:50) (BD Biosciences, 562077) or anti-STAT1 pY701 (1:50) (BD Biosciences, 612564) and human TruStain FcX (1:100) (Biolegend, 422302) for 1 hour at RT. Cells were washed with PBE and acquired on a SONY SA3800 flow cytometer. Data were analysed using FlowJo software version 10.6 software (Tree Star). pSTAT signal was measured as a function of mean fluorescence intensity (MFI). Percent max signal was calculated by subtracting background MFI and calculating values as a percentage of cytokine induced pSTAT MFI in the absence of IgG. Curves were fit using a sigmoidal 4 parameter logistic curve.

Functional validation of anti-CXCL1, anti-CXCL7, and anti-HCRTR2 autoantibodies

CXCL1, CXCL7, and orexin signaling was assayed using the PRESTO-TANGO system[37,38–40]. HTLA cells, a HEK293-derived cell line that stably expresses β-arrestin-TEV and tTA-Luciferase, were seeded in wells of a sterile tissue culture grade flat bottom 96-well plate (35,000 cells/well) in 100 µL DMEM (+ 10% FBS, 1% Penicillin/Streptomycin) and incubated at 37 °C, 5% CO_2. 18-24 hr after seeding (approximately 80-90% cell confluence), 200 ng CXCR2-Tango or HCTR2-Tango plasmid in 20 µL DMEM and 600 ng Polyethylenimine-Max (Polysciences, 24765-1) in 20 µL DMEM were mixed, incubated at room temperature for 20 min, and added to each well. 18-24 hr after transfection, medium

was replaced with 100 µL DMEM (+ 1% Penicillin/Streptomycin, 10 mM HEPES) containing 10 ng CXCL7 (Peprotech, 300-14) or CXCL1 (PeproTech, 300-46), or 100 nM orexin A (Millipore Sigma, O6012) and 5 µg isolated IgG. IgG was purified from plasma using protein G magnetic beads (Lytic Solutions) as previously described[7]. 18-24 hr after stimulation, supernatant was replaced with 50 µL Bright-Glo solution (Promega) diluted 20-fold with PBS with 20 mM HEPES. The plate was incubated at room temperature for 20 min in the dark and luminescence was quantified using a Synergy HTX Multi-Mode Microplate Reader (BioTek). HTLA cells were a gift from Noah Palm. Tango plasmids were a gift from Bryan Roth (Addgene plasmid # 66260)

Functional validation of anti-CD38 and anti-CD3ε autoantibodies

Bone marrow stem cells were isolated from 8-week old C57BL/6 mouse femur and tibia. Cells were plated in RPMI (+ 10% heat inactivated FBS, 10 U/mL Penicillin, 100 mg/mL Streptomycin; cRPMI) with 30% (vol/vol) L929 fibroblast conditioned media as a source of M-CSF and incubated at 37 °C, 5% CO_2. On day 3 post-isolation, 10 mL L929 fibroblast conditioned media was added to plates. 200,000 BMDMs (7 days post isolation) were plated on non-TC treated 6-well plates in cRPMI + 10% L929 media. The following day, Raji (ATCC, CCL-86) or Jurkat (ATCC, TIB-152) cells were labelled using CellTrace Far Red (Thermo Fisher) according to standard manufacturer protocols. For the T cell ADCP assay, labelled Jurkat cells were incubated with 100 µg/mL healthy control IgG or CD3ε AAb^+ patient IgG for 30 minutes on ice. Mouse IgG2a anti-human CD3ε (clone OKT3, Biolegend) was used at 5 µg/mL as a positive control. Jurkat cells were washed with 10 ml PBS. 10^6 Jurkat cells were added to each well and incubated for 3 hours. For the B cell ADCP assay, Raji cells were incubated with complement inactivated patient plasma at 1:50 dilution in PBS for 30 minutes on ice. Mouse IgG2a anti-human CD38 (clone MAB2404, R&D systems) was used at 5 µg/mL as a positive control. Raji cells were washed with 10 mL PBS once. 500,000 Raji cells were added to each well and incubated for 3 hours at 37 °C, 5% CO_2. BMDMs were detached from the plate after a 3-hour incubation using 10 mM EDTA PBS and stained with anti-mouse CD45 – Pacific blue (clone 30-F11, Biolegend) for 30 minutes at 4 °C. Samples were acquired on a CytoFLEX flow cytometer (Beckman Coulter).

Mice

B6.Cg-Tg(K18-ACE2)2Prlmn/J (K18-hACE2) mice (Stock #: 034860) and C57BL/6 mice (Stock #: 000664) were purchased from the Jackson Laboratories and were subsequently bred and housed at Yale University. 6- to 10-week-old mixed sex mice were used throughout the study. All mice were housed as groups of 5 to 6 individuals per cage and maintained on a 12-hour light/dark cycle (lights on at 7:00 AM) at 22–25 °C temperature and 30–70% relative humidity under specific-pathogen free conditions. All procedures used in this study (sex-matched, age-matched) complied with federal guidelines and the institutional policies of the Yale School of Medicine Animal Care and Use Committee.

SARS-CoV-2 mouse infections and antibody treatments

Before infection, mice were anesthetized using 30% (vol/vol) isoflurane diluted in propylene glycol. 50 µL of SARS-CoV-2 isolate USA-WA1/2020 (NR-52281; BEI Resources) at 2×10^4 or 6×10^4 PFU/mL was delivered intranasally to mice, equivalent of 1,000 (sublethal dose) or 3,000 (median lethal dose) PFU/mouse, respectively. Following infection, weight loss and survival were monitored daily. For IFNAR blockade, mice were treated once with 2 mg of blocking antibodies one day prior to infection (Clone MAR1-5A3). For IL-18 blockade, mice were treated three times each with 0.5 mg of blocking antibodies at day 0, 2, and 4 day post infection (Clone YIGIF74-1G7). For blockade of IL-1β, GM-CSF, or IL-21R, mice were treated three times each with 0.2 mg of blocking antibodies at day 0, 2, and 4 day post infection (Anti-IL-1β: Clone B122; anti-GM-CSF: Clone MP1-22E9; anti-IL-21R: clone 4A9). The first injection of anti-IL18, anti-IL-1β, anti-GM-CSF, or anti-IL-21R antibodies was given at least 8 to 10 hours before infection. All blocking antibodies were purchased from BioXCell.

Statistical analysis

Details of linear models and principal component analysis can be found in Supplementary Methods. Specific details of other statistical analysis are found in relevant figure legends. Data analysis was performed using MATLAB, GraphPad Prism, R, and the following R packages: ggplot2, edgeR, tidyverse, tidyr, dplyr, stringr, forcats, lme4, emmeans, and ggpubr.

Reporting summary

Further information on research design is available in the Nature Research Reporting Summary linked to this paper.

Data availability

Published RNA-seq dataset is publicly available at https://www.ncbi.nlm.nih.gov/geo/query/acc.cgi?acc=GSE107011 (GEO: GSE107011). All data analyzed in this study are available in the Article, the Source Data files, or the Supplementary Information. Data not available within the manuscript are available from the corresponding author upon reasonable request. Source data are provided with this paper.

Code availability

Custom codes used for analysis in this study are available publicly at https://github.com/ring-lab/COVID-19_REAP_nature_2021.

32. Wyllie, A. L. *et al*. Saliva or Nasopharyngeal Swab Specimens for Detection of SARS-CoV-2. *N. Engl. J. Med*. **383**, 1283–1286 (2020).
33. McPadden, J. *et al*. Health Care and Precision Medicine Research: Analysis of a Scalable Data Science Platform. *J. Med. Internet Res*. **21**, e13043 (2019).
34. Schulz, W. L., Durant, T. J. S., Torre, C. J., Jr, Hsiao, A. L. & Krumholz, H. M. Agile Health Care Analytics: Enabling Real-Time Disease Surveillance With a Computational Health Platform. *J. Med. Internet Res*. **22**, e18707 (2020).
35. McPadden, J. *et al*. Clinical Characteristics and Outcomes for 7,995 Patients with SARS-CoV-2 Infection. *medRxiv* (2020) https://doi.org/10.1101/2020.07.19.20157305.
36. Robinson, M. D., McCarthy, D. J. & Smyth, G. K. edgeR: a Bioconductor package for differential expression analysis of digital gene expression data. *Bioinformatics* **26**, 139–140 (2010).
37. Kroeze, W. K. *et al*. PRESTO-Tango as an open-source resource for interrogation of the druggable human GPCRome. *Nat. Struct. Mol. Biol*. **22**, 362–369 (2015).
38. Amanat, F. *et al*. A serological assay to detect SARS-CoV-2 seroconversion in humans. *Nat. Med*. **26**, 1033–1036 (2020).
39. Vogels, C. B. F. *et al*. Analytical sensitivity and efficiency comparisons of SARS-CoV-2 RT-qPCR primer-probe sets. *Nat Microbiol* **5**, 1299–1305 (2020).
40. Israelow, B. *et al*. Mouse model of SARS-CoV-2 reveals inflammatory role of type I interferon signaling. *J. Exp. Med*. **217**, (2020).

Acknowledgements The authors gratefully acknowledge all members of the Ring and Iwasaki labs and also Eric Meffre, Joseph Craft, and Kevin O'Connor for helpful conversation and technical assistance. Melissa Linehan and Huiping Dong provided logistical assistance and H. Patrick Young provided technical assistance with data management. We thank Neil K. Savalia and Tyler J. Shelby for discussion regarding statistical techniques. The authors also thank Dr. Lawrence Steinman for helpful discussions about autoantibodies to HCRTR2. This work was supported by the Mathers Family Foundation (to A.M.R. and A.I.), the Ludwig Family Foundation (to A.M.R. and A.I.), a supplement to the Yale Cancer Center Support Grant 3P30CA016359-40S4 (to A.M.R.), the Beatrice Neuwirth Foundation, Yale Schools of Medicine and Public Health and NIAID grant U19 AI08992. IMPACT received support from the Yale COVID-19 Research Resource Fund. A.M.R. is additionally supported by an NIH Director's Early Independence Award (DP5OD023088), a Pew-Stewart Award, and the Robert T. McCluskey Foundation. T.M. and Y.D. are supported by the Yale Interdisciplinary Immunology Training Program T32AI007019. J.K. and J.R.J. are supported by the Yale Medical Scientist Training Program T32GM007205.

Author contributions E.Y.W., T.M., J.K., Y.D., J.D.H., J.R.J., A.I., and A.M.R. designed experiments. E.Y.W. and Y.D. performed the REAP assay. E.Y.W., Y.D., J.D.H., J.R.J., F.L., E.S.P., and S.F. performed biochemical and functional validations. T.M., B.I., and E.S. performed mouse experiments. C.L., P.W., J.K., J.S., T.M., and J.E.O. defined parameters for flow cytometry experiments, collected and processed patient PBMC samples. A.L.W., C.B.F.V., I.M.O., C.C.K., M.E.P., and A.E.W. performed the virus RNA concentration assays. N.D.G. supervised the virus RNA concentration assays. B.I. and J.K. collected epidemiological and clinical data. C.D.C., S.F., A.I.K., M.C., and J.F. assisted in designing, recruiting, and following in-patient and HCW

cohorts. A.C. performed clinical data aggregation and management. W.L.S. supervised clinical data aggregation and management. E.Y.W., T.M., J.K., N.S.Z., Y.D., J.D.H., J.R.J., A.I., and A.M.R. analyzed data. S.M. supervised the statistical analysis. E.Y.W., T.M., J.K., A.I., and A.M.R. wrote the paper. A.M.R. and A.I. supervised the research. Authors from the Yale IMPACT Research Team contributed to collection and storage of patient samples, as well as the collection of the patients' epidemiological and clinical data.

Competing interests A.M.R., E.Y.W., and Y.D. are inventors of a pending patent application (PCT/US21/23521) filed by Yale University describing the REAP technology used in this paper. A.M.R. is the founder of Seranova Bio, the commercial licensee of the REAP technology. A.I. serves as a consultant for Spring Discovery, Boehringer Ingelheim, and Adaptive Biotechnologies.

Additional information

Supplementary information The online version contains supplementary material available at https://doi.org/10.1038/s41586-021-03631-y.

Correspondence and requests for materials should be addressed to A.I. or A.M.R.

Peer review information *Nature* thanks Petter Brodin, Karl Dane Wittrup and the other, anonymous, reviewer(s) for their contribution to the peer review of this work. Peer reviewer reports are available.

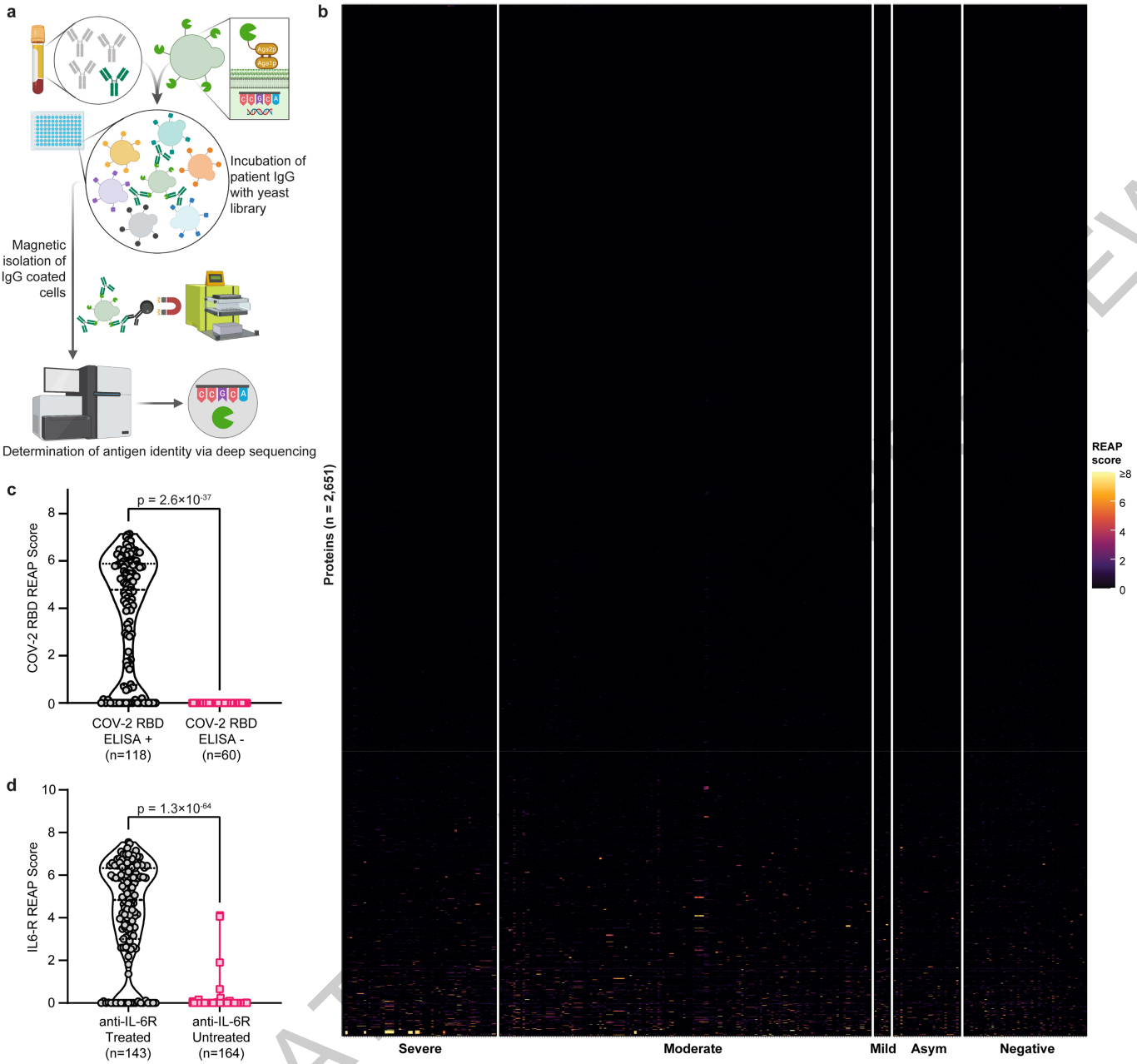

Extended Data Fig. 1 | REAP screen of COVID-19 patients. a, A simplified schematic of REAP. Antibodies are incubated with a barcoded yeast library displaying members of the exoproteome. Antibody bound yeast are enriched by magnetic column-based sorting and enrichment is quantified by next-generation sequencing. Schematic was created with Biorender.com. **b**, Heatmap of all profiled reactivities across all patient samples stratified by disease severity and using the same color scale as in Figure 1a. Sticky antigens (as defined in Methods) were removed from the heatmap. **c**, SARS-CoV-2 RBD REAP scores for COVID-19 patient samples stratified by positive or negative ELISA RBD reactivity. **d**, IL-6-R REAP scores for COVID-19 patient samples stratified by treatment with an anti-IL-6R biologic therapy (tocilizumab or sarilumab). Samples collected at least one day after infusion were considered treated. Samples collected on the day of infusion were excluded from analysis due to uncertainty in the timing of sample collection. Significance in **c,d** was determined using a linear mixed model (see Methods). In **c,d** *n* values include longitudinal samples from the same patient.

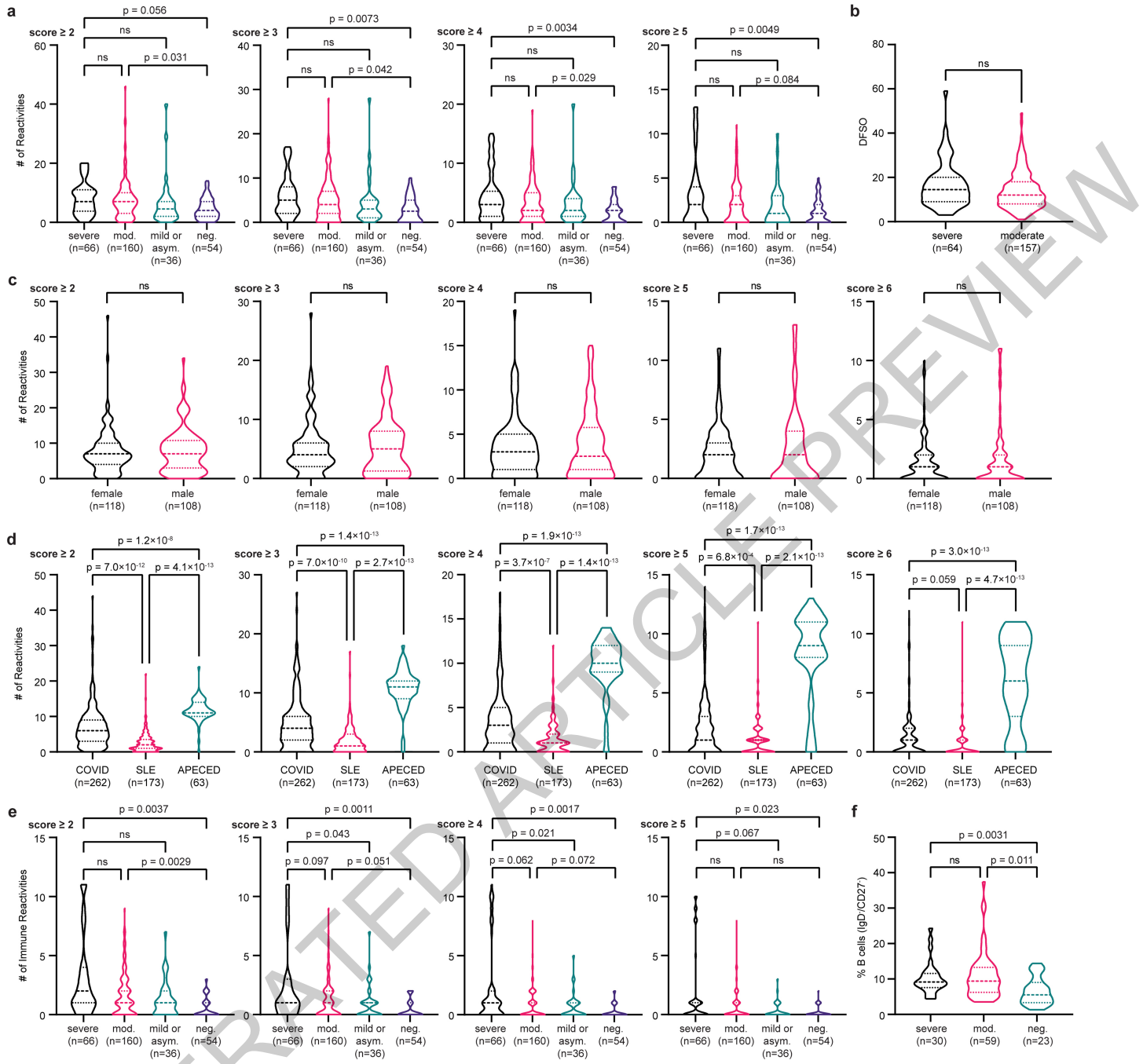

Extended Data Fig. 2 | Comparisons of reactivities and clinical/immunological parameters between patient groups. a, Number of positive reactivities per sample at various REAP score cutoffs, stratified by disease severity. **b**, Days from symptom onset (DFSO) in severe and moderate COVID-19 samples. DFSO data was not available for a limited number of samples from each group and was not available for any mild or asymptomatic COVID-19 samples. The median (solid line) and first and third quartile (dashed lines) are shown. **c**, Number of positive reactivities per sample at various REAP score cutoffs, stratified by patient sex. **d**, Number of positive reactivities in COVID-19, SLE, and APECED patient samples at various score cutoffs. SLE and APECED patients were screened as previously described[7]. Due to the smaller size of the yeast exoproteome library used to screen the SLE and APECED samples, reactivities in COVID-19 samples against proteins that were not in the previously described yeast exoproteome library were removed from these analyses. **e**, Number of positive immune-targeting reactivities per sample at various REAP score cutoffs, stratified by disease severity. **f**, Average percentages of IgD-/CD27- B cells among peripheral leukocytes in COVID-19 patients stratified by disease severity and uninfected controls (neg.). In **a**-**e** *n* values include longitudinal samples from the same patient. In **f** *n* values indicate samples from unique patients. Significance was determined using linear mixed models (**a**-**e**; see Methods) or a Kruskal-Wallis test followed by a two-sided Dunn's test (**f**). Medians are represented by a dashed line and first/third quartiles are represented by dotted lines for all plots in this figure.

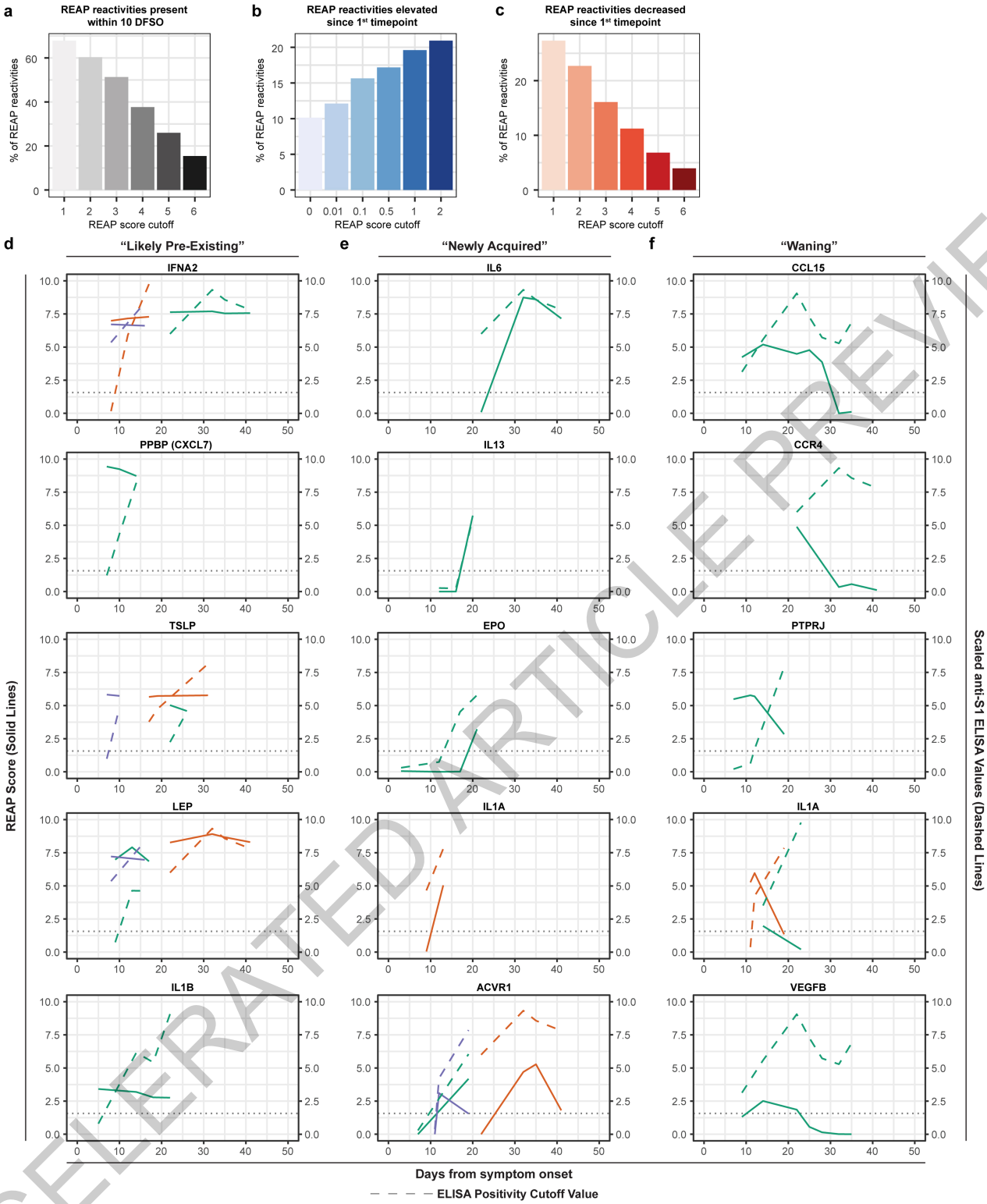

Extended Data Fig. 3 | Autoantibodies exhibit varied developmental kinetics in COVID-19 patients. a, Percentage of reactivities (REAP score greater than score cutoff) in COVID-19 patients present within 10 days from symptom onset at various score cutoffs. **b**, Percentage of reactivities in COVID-19 patients that had a REAP score less than the score cutoff (using various score cutoffs) at the first time point sampled and an increase in REAP score of at least 1 at the last time point. **c**, Percentage of reactivities in COVID-19 patients that had a REAP score greater than the score cutoff (using various score cutoffs) at the first time point sampled and a decrease in REAP score of at least 1 at the last time point. For **a-c**, all COVID-19 patients with longitudinal samples available (n=77 patients) were included in calculations. **d-f**, Plots of longitudinal changes in REAP score for "likely pre-existing" (**d**), "newly acquired" (**e**), and "waning" (**f**) REAP reactivities in individual patients alongside scaled anti-spike S1 ELISA values in the same patients. Scaled ELISA values are defined as anti-spike S1 ELISA OD (450 nm - 570 nm) values multiplied by four. In each plot, unique patients are represented by uniquely colored lines. For a given patient, solid lines connect REAP scores of reactivities against respective antigens at various time points and dashed lines connect scaled anti-spike S1 ELISA values at those same time points. The dotted grey line indicates the scaled ELISA positivity cutoff value (see Methods).

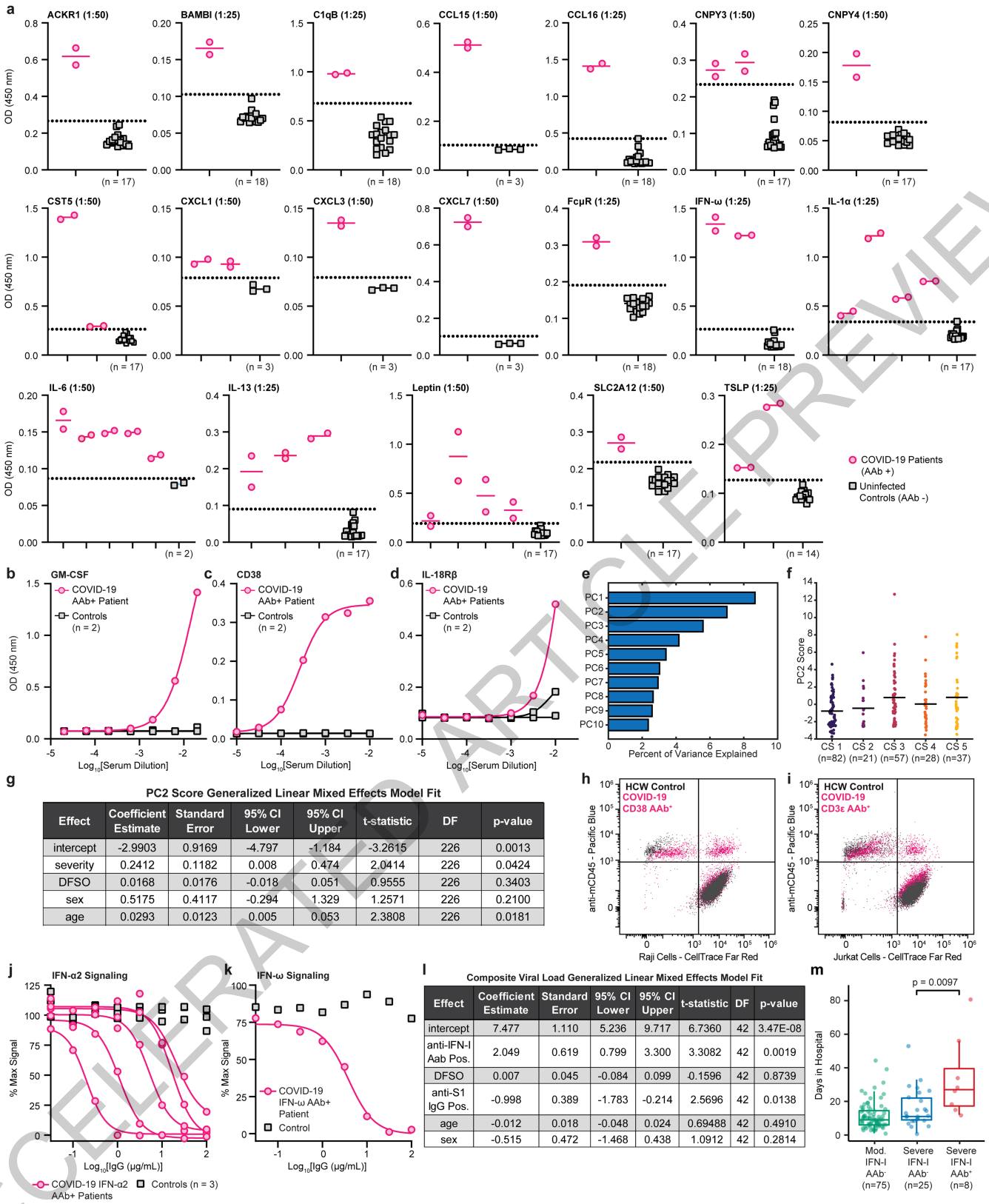

g

PC2 Score Generalized Linear Mixed Effects Model Fit

Effect	Coefficient Estimate	Standard Error	95% CI Lower	95% CI Upper	t-statistic	DF	p-value
intercept	-2.9903	0.9169	-4.797	-1.184	-3.2615	226	0.0013
severity	0.2412	0.1182	0.008	0.474	2.0414	226	0.0424
DFSO	0.0168	0.0176	-0.018	0.051	0.9555	226	0.3403
sex	0.5175	0.4117	-0.294	1.329	1.2571	226	0.2100
age	0.0293	0.0123	0.005	0.053	2.3808	226	0.0181

l

Composite Viral Load Generalized Linear Mixed Effects Model Fit

Effect	Coefficient Estimate	Standard Error	95% CI Lower	95% CI Upper	t-statistic	DF	p-value
intercept	7.477	1.110	5.236	9.717	6.7360	42	3.47E-08
anti-IFN-I Aab Pos.	2.049	0.619	0.799	3.300	3.3082	42	0.0019
DFSO	0.007	0.045	-0.084	0.099	0.1596	42	0.8739
anti-S1 IgG Pos.	-0.998	0.389	-1.783	-0.214	2.5696	42	0.0138
age	-0.012	0.018	-0.048	0.024	0.69488	42	0.4910
sex	-0.515	0.472	-1.468	0.438	1.0912	42	0.2814

Extended Data Fig. 4 | See next page for caption.

Extended Data Fig. 4 | Biochemical and functional validation of autoantibodies in COVID-19 patients. a, Single point pan-IgG autoantibody ELISAs conducted with 1:25 or 1:50 plasma dilution (indicated in graph titles). Dotted line represents the uninfected control (healthcare worker) average plus 3 standard deviations. For controls, results (averages of technical duplicates) from biologically independent samples are displayed in the same column (*n* indicated below each column). For COVID-19 patients, results from one patient are displayed in each column and technical duplicates are depicted as distinct points. **b**, GM-CSF, **c**, CD38, and **d**, IL-18Rβ pan-IgG autoantibody ELISAs conducted with serial dilutions of COVID-19 patient or uninfected control plasma. Results are averages of 2 technical replicates. Curves were fit using a sigmoidal 4 parameter logistic curve. Experiments in **a-d** were performed once. **e**, Percent of variance explained for principal components from the principal component analysis in Figure 1d. **f**, PC2 scores of COVID-19 samples stratified by clinical score (CS). Solid black lines depict group means. **g**, Fixed effects model fits from a generalized linear mixed effects model with PC2 score as the dependent variable (details in Methods). **h,i** Flow cytometry gating for the Raji (**h**) and Jurkat (**i**) macrophage phagocytosis assay in Figure 2c. **j,k** IFN-α2 (**j**) and IFN-ω (**k**) signaling assay performed with anti-IFN-α2 or anti-IFN-ω autoantibody positive COVID-19 patient IgG and uninfected control IgG. Results are averages of 2 technical replicates from one experiment. **l**, Fixed effects model fits for the generalized linear mixed effects model in Figure 2d (details in Methods). **m**, Hospital stay length in patients with and without anti-IFN-I autoantibodies, stratified by disease severity. Significance in **m** was determined using a two-sided Wilcoxon rank-sum test. In **f**, *n* values include longitudinal samples from the same patient. All other *n* values in this figure indicate samples from unique patients.

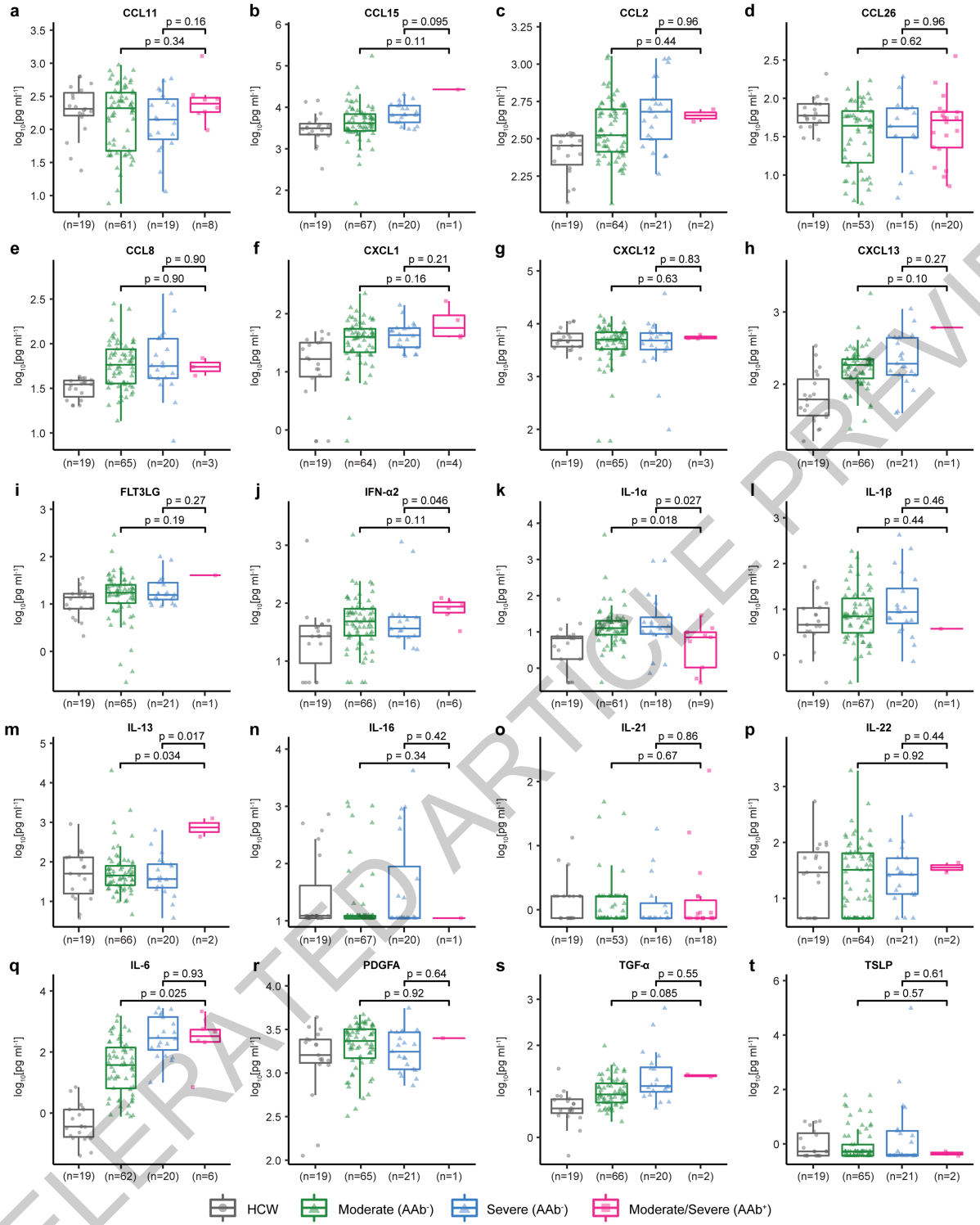

Extended Data Fig. 5 | Effects of anti-cytokine autoantibodies on corresponding cytokine plasma concentrations. a-t, Average concentration of plasma CCL11 (**a**), CCL15 (**b**), CCL2 (**c**), CCL26 (**d**), CCL8 (**e**), CXCL1 (**f**), CXCL12 (**g**), CXCL13 (**h**), FLT3LG (**i**), IFNA2 (**j**), IL1A (**k**), IL1B (**l**), IL13 (**m**), IL16 (**n**) and IL21 (**o**), IL22 (**p**), IL6 (**q**), PDGFA (**r**), TGFA (**s**), and TSLP (**t**) measured by a Luminex assay in patients stratified by COVID-19 disease severity and REAP reactivity (AAb^+; REAP score ≥ 2 at any time point) against the corresponding cytokine. Data are presented as boxplots with the first quartile, median, third quartile, whiskers (minimum/maximum value within the first or third quartile ± 1.5 times the interquartile range), and individual data points indicated. Significance was determined using two-sided, Wilcoxon rank-sum tests. All *n* values in this figure indicate samples from unique patients.

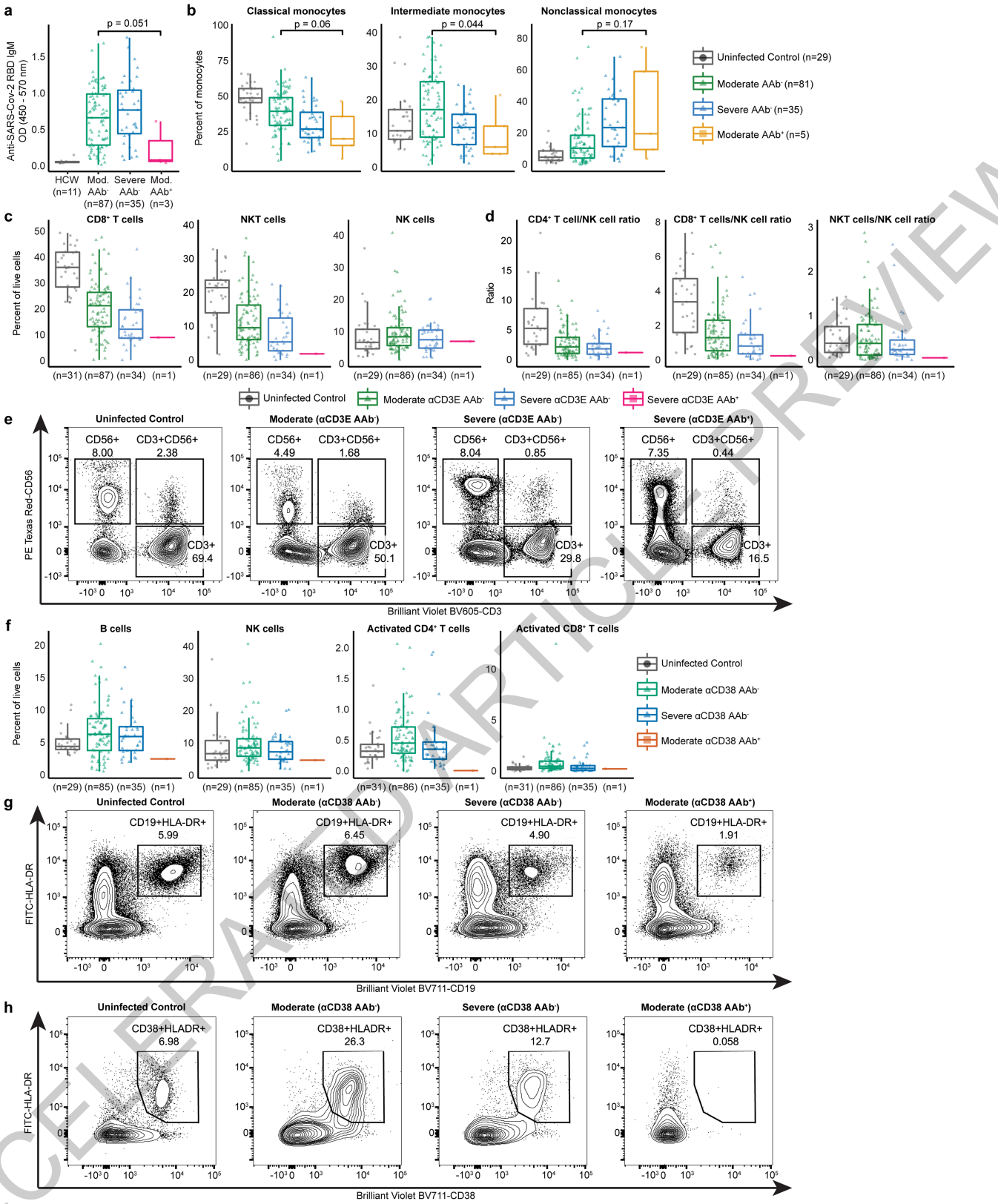

Extended Data Fig. 6 | See next page for caption.

Extended Data Fig. 6 | Additional immune cell surface targeting autoantibody correlations. a, Average anti-SARS-CoV-2 RBD IgM reactivity as measured by ELISA in patients stratified by COVID-19 disease severity and REAP reactivity against B cell displayed proteins (as defined in Figure 2e). **b**, Average percentage among total monocytes of classical monocytes, intermediate monocytes, and nonclassical monocytes in patients stratified by COVID-19 disease severity and REAP reactivity against proteins preferentially displayed on classical/intermediate monocyte (as defined in Figure 2f). **c**, Average percent $CD8^+$ T cells, NKT cells, and NK cells among peripheral leukocytes in patients stratified by COVID-19 disease severity and REAP reactivity against CD3ε. **d**, Average $CD4^+$ T cell to NK cell ratio, $CD8^+$ T cell to NK cell ratio, and NKT cell to NK cell ratio among peripheral leukocytes in patients stratified by COVID-19 disease severity and REAP reactivity against CD3ε. **e**, Representative flow plot of T cells ($CD3^+$), NK cells ($CD56^+$), and NKT cells ($CD3^+CD56^+$) for Extended Data Figure 6c,d. f, Average percent B cells, NK cells, activated $CD4^+$ T cells, and activated $CD8^+$ T cells among peripheral leukocytes in patients stratified by COVID-19 disease severity and REAP reactivity against CD38. **g**, Representative flow plot of B cells ($CD19^+$HLA-DR^+) for Extended Data Figure 6f. h, Representative flow plot of activated $CD8^+$ T cells ($CD38^+$HLA-DR^+) for Extended Data Figure 6f. Significance in **a** was determined using a two-sided Wilcoxon rank-sum test. All *n* values in this figure indicate samples from unique patients. All boxplots are presented with the median, first and third quartile, whiskers (minimum/maximum value within the first or third quartile ± 1.5 times the interquartile range), and individual data points indicated.

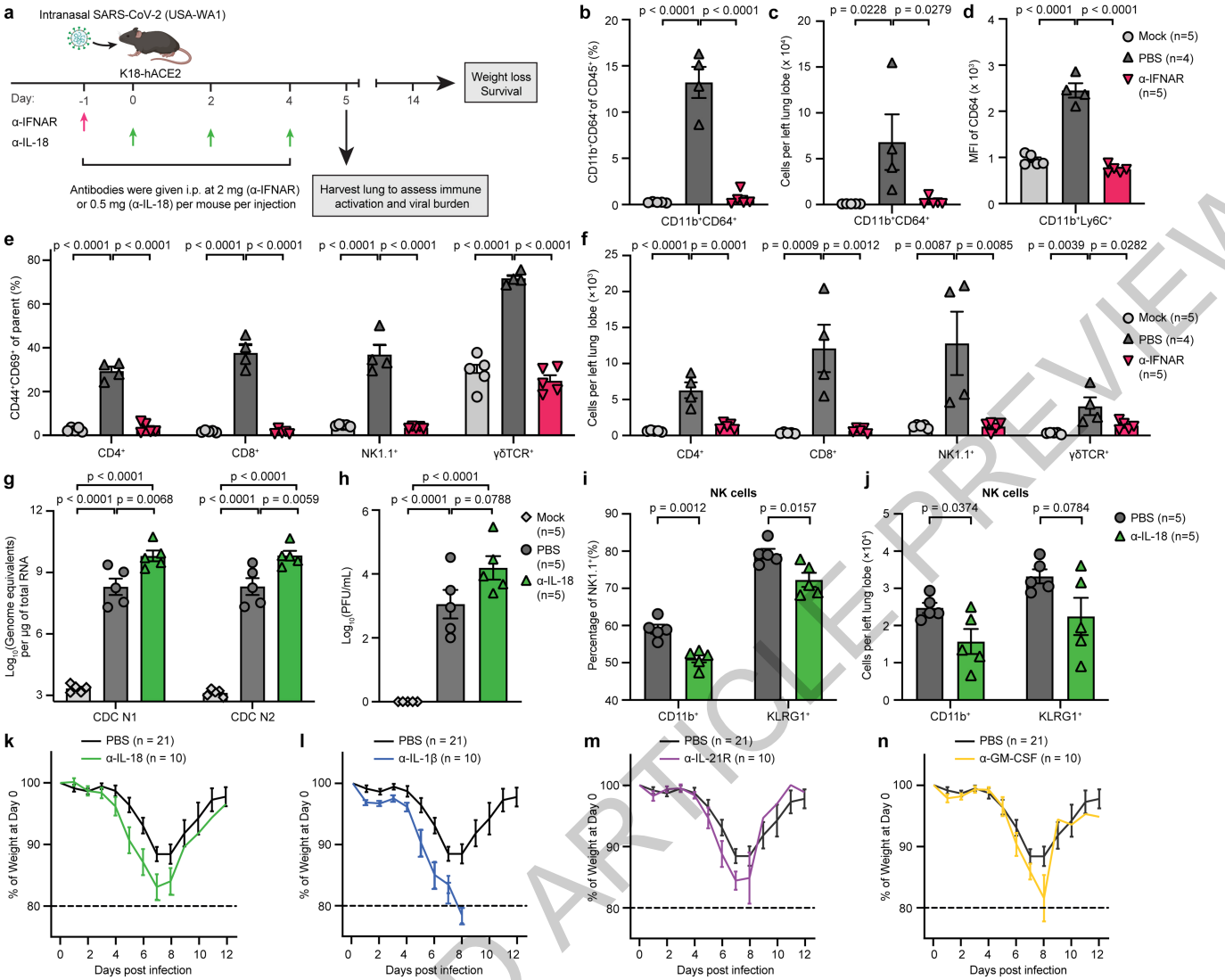

Extended Data Fig. 7 | Additional immunological and clinical characterization of autoantibody effects in a COVID-19 mouse model. **a**, K18-hACE2 mice were intranasally infected with sublethal dose (**b-f**) or median lethal dose (**g-n**) of SARS-CoV-2 (USA-WA1/2020 isolate) and treated with indicated antibodies. **b,c**, Relative frequency (**b**) and absolute number (**c**) of lung Ly6C$^+$CD11b$^+$CD64$^+$ macrophages from mock-infected, SARS-CoV-2-infected PBS-treated, and SARS-CoV-2-infected α-IFNAR-treated K18 mice. **d**, Expression of CD64 on lung-infiltrating CD11b$^+$Ly6C^{high} monocytes. **e,f**, Relative frequency (**e**) and absolute number (**f**) of CD44$^+$CD69$^+$ lymphocytes (CD4$^+$ T cells, CD8$^+$ T cells, NK1.1$^+$ cells, and γδ T cells). **g,h**, Viral RNA loads (**g**) and infectious titers (**h**) from lung tissue homogenates of mock-infected, SARS-CoV-2-infected PBS-treated, and SARS-CoV-2-infected α-IL-18-treated mice measured by RT-qPCR and plaque assay, respectively. **i,j**, Relative frequency (**i**) or absolute number (**j**) of CD11b$^+$ and KLRG1$^+$ NK1.1$^+$ cells in lung tissues of PBS and α-IL-18-treated mice. **k-n**, Normalized body weight of α-IL-18 (**k**), α-IL-1β (**l**), α-IL-21R (**m**), α-GM-CSF (**n**), and PBS-treated K18 mice from day 1 to 14 post infection. Significance was determined using one-way ANOVA followed by Tukey correction (**b-f, g**), and unpaired two-tailed t tests (**i,j**). All *n* values in this figure represent biologically independent animals examined over 2 independent experiments.

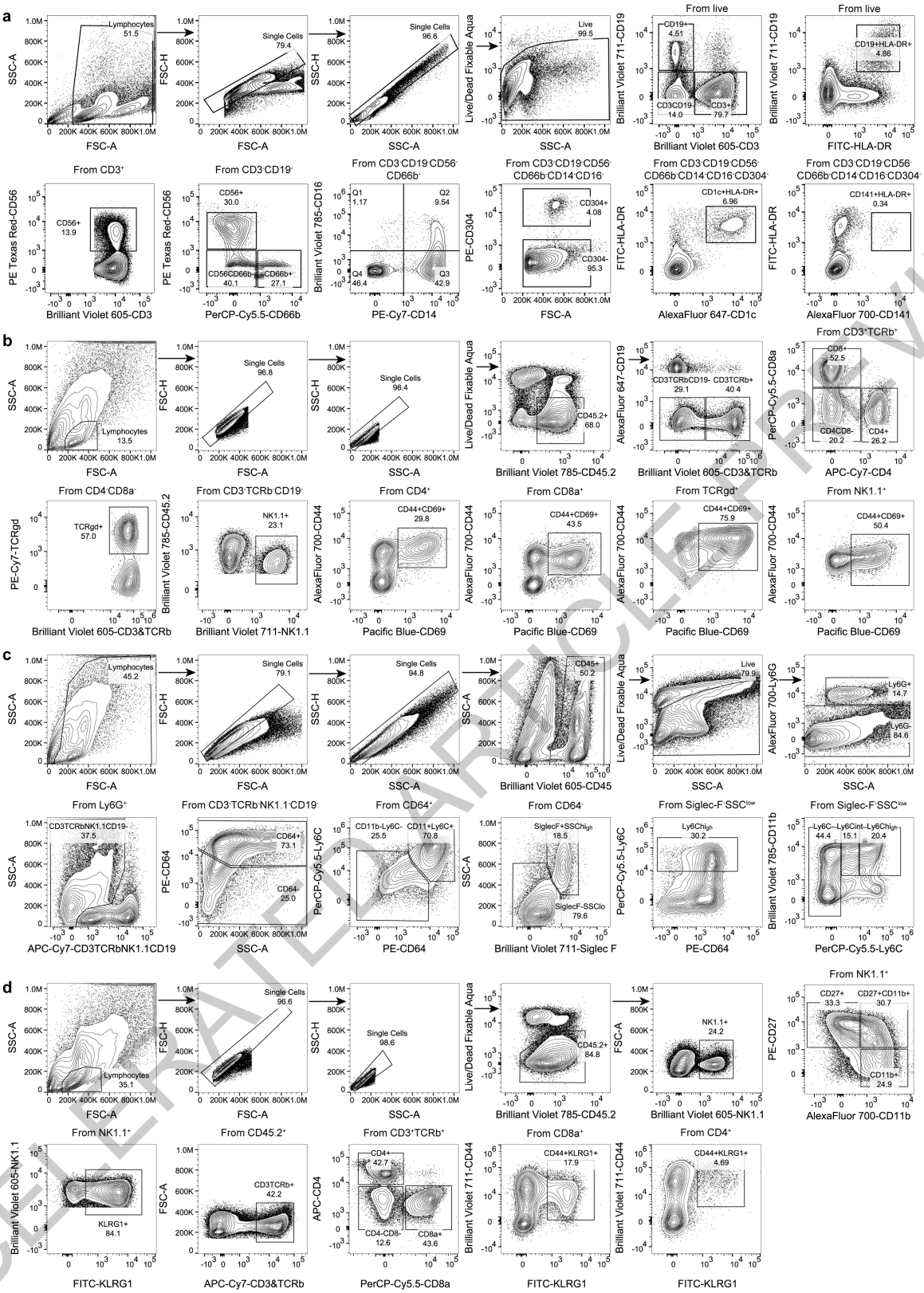

Extended Data Fig. 8 | Flow cytometry gating strategies for immunophenotyping experiments. a, Gating strategy to identify B cells described in Figure 2e, monocytes described in Figure 2f & Extended Data Figure 6b, and T cells/NKT cells/NK cells described in Figure 2g, Extended Data Figure 6c,d,f, in human PBMCs. **b**, Gating strategy to identify CD11b^{+}Ly6C^{high} monocytes and Ly6C^{+}CD11b^{+}CD64^{+} macrophages in mouse lung tissues described in Extended Data Figure 7b-d. c, Gating strategy to identify CD44^{+}CD69^{+} lymphocytes in mouse lung tissues described in Extended Data Figure 7e,f. d, Gating strategy to identify KLRG1^{+} and CD11b^{+} NK cells described in Extended Data Figure 7i,j.

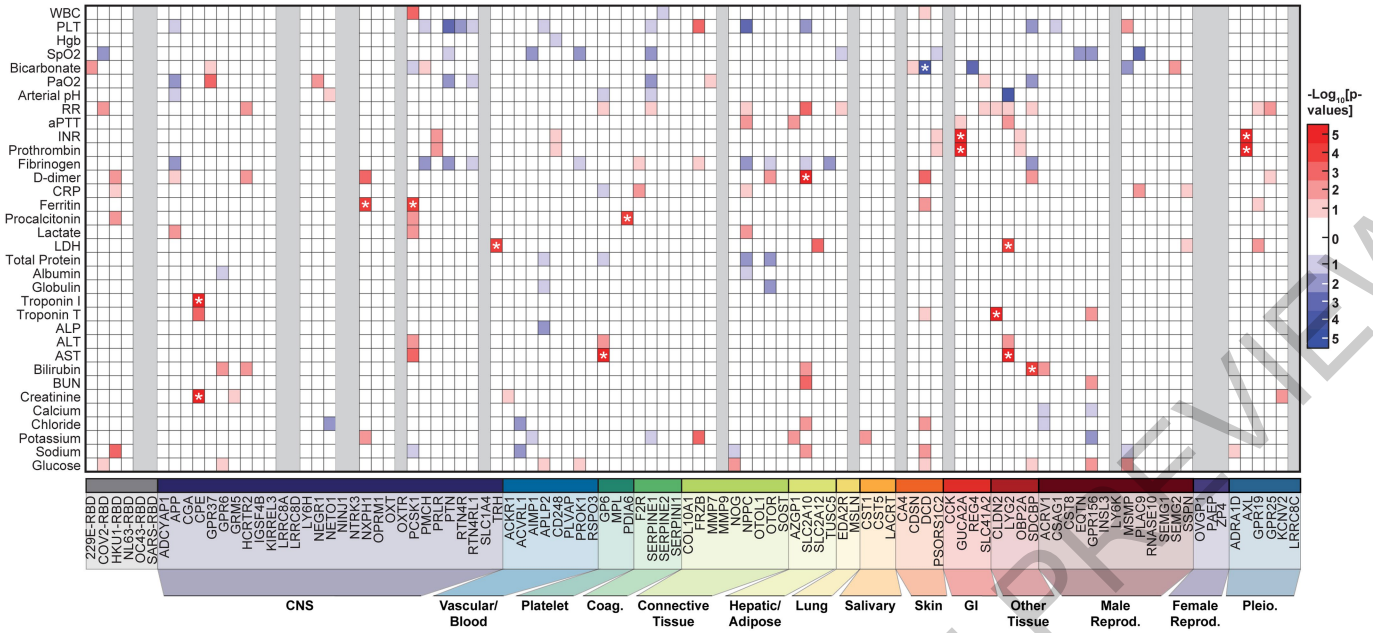

Extended Data Fig. 9 | Tissue-associated autoantibodies are correlated with clinical parameters in COVID-19 patients. Heatmap of pairwise, -$\log_{10}$ transformed REAP protein p-values from generalized linear model (GLM) fits accounting for age, sex, and maximum REAP score in estimating average or minimum clinical values from hospital admission. A total of 135 samples from unique patients were included in this analysis (n=135). Intensity represents p-values and color indicates directionality of gene-parameter pairs (red indicates positive change, blue indicates negative change. Grey columns indicate genes excluded from analysis due to insufficient patient number (n<2). Asterisks denote pairwise relationships that were significant after correction for multiple comparisons (FDR). Specific details of the GLMs can be found in the Methods. Proteins were classified as in Figure 4a.

Extended Data Table 1 | IMPACT cohort patient demographics and clinical characteristics

	Severe	Moderate	Mild	Asymptomatic	Negative	Total
n	55	103	7	29	54	248
Age (years)	63.15 ± 17.79	64.56 ± 15.77	35.14 ± 14.48	46.55 ± 19.82	39.17 ± 12.28	56.05 ± 19.43
Sex (M|F)	30 (54%) | 25 (46%); n=55	49 (48%) | 54 (52%); n=103	0 (54%) | 7 (100%); n=7	8 (36%%) | 14 (64%); n=22	25 (46%) | 29 (54%); n=54	112 (46%) | 129 (54%); n=241
BMI	32.25 ± 8.8; n=50	30.48 ± 8.28; n=97	--	28.88 ± 8.1; n=18	--	30.84 ± 8.44; n=176
COVID Risk Factors						
None	13 (24%)	25 (24%)	--	--	--	38 (24%); n=158
Cancer (<1 year)	5 (9%)	6 (6%)	--	--	--	11 (7%); n=158
Chronic Heart Disease	15 (27%)	30 (29%)	--	--	--	45 (28%); n=158
Hypertension	28 (51%)	55 (53%)	--	--	--	83 (53%); n=158
Chronic Lung Disese	9 (16%)	25 (24%)	--	--	--	34 (22%); n=158
Immunosuppresion	4 (7%)	9 (9%)	--	--	--	13 (8%); n=158

nature research

Corresponding author(s): Aaron Ring, Akiko Iwasaki

Last updated by author(s): May 4, 2021

Reporting Summary

Nature Research wishes to improve the reproducibility of the work that we publish. This form provides structure for consistency and transparency in reporting. For further information on Nature Research policies, see our Editorial Policies and the Editorial Policy Checklist.

Statistics

For all statistical analyses, confirm that the following items are present in the figure legend, table legend, main text, or Methods section.

n/a	Confirmed	
☐	☒	The exact sample size (*n*) for each experimental group/condition, given as a discrete number and unit of measurement
☐	☒	A statement on whether measurements were taken from distinct samples or whether the same sample was measured repeatedly
☐	☒	The statistical test(s) used AND whether they are one- or two-sided *Only common tests should be described solely by name; describe more complex techniques in the Methods section.*
☒	☐	A description of all covariates tested
☐	☒	A description of any assumptions or corrections, such as tests of normality and adjustment for multiple comparisons
☐	☒	A full description of the statistical parameters including central tendency (e.g. means) or other basic estimates (e.g. regression coefficient) AND variation (e.g. standard deviation) or associated estimates of uncertainty (e.g. confidence intervals)
☐	☒	For null hypothesis testing, the test statistic (e.g. *F*, *t*, *r*) with confidence intervals, effect sizes, degrees of freedom and *P* value noted *Give P values as exact values whenever suitable.*
☒	☐	For Bayesian analysis, information on the choice of priors and Markov chain Monte Carlo settings
☒	☐	For hierarchical and complex designs, identification of the appropriate level for tests and full reporting of outcomes
☐	☒	Estimates of effect sizes (e.g. Cohen's *d*, Pearson's *r*), indicating how they were calculated

Our web collection on statistics for biologists contains articles on many of the points above.

Software and code

Policy information about availability of computer code

Data collection	EPIC EHR software (retrospective EMR review and clinical data aggregation) and REDCap 9.3.6 (clinical data aggregation).
Data analysis	R (version 4.0.2), tidyverse (version 1.3.0), ggplot2 (version 3.3.2), edgeR (version 3.30.3), tidyr (version 1.1.1), dplyr (version 1.0.1), forcats (version 0.5.0), pheatmap (version 1.0.8), ggpubr (0.1.6), stringr (1.4.0), lme4 (1.1-23), emmeans (1.5.4), MATLAB (9.10), GraphPad Prism (version 9.0.0), FlowJo (version 10.6, Tree Star), Attune NxT (version 3.1.2)

For manuscripts utilizing custom algorithms or software that are central to the research but not yet described in published literature, software must be made available to editors and reviewers. We strongly encourage code deposition in a community repository (e.g. GitHub). See the Nature Research guidelines for submitting code & software for further information.

Data

Policy information about availability of data

All manuscripts must include a data availability statement. This statement should provide the following information, where applicable:

- Accession codes, unique identifiers, or web links for publicly available datasets
- A list of figures that have associated raw data
- A description of any restrictions on data availability

All human peripheral blood flow cytometry data has previously been made available via ImmPort website (study ID: SDY1648). All data used to generate figures and tables in this study are either included in the Supplementary Information Table 1 or available from the corresponding authors upon reasonable request.

Field-specific reporting

Please select the one below that is the best fit for your research. If you are not sure, read the appropriate sections before making your selection.

☒ Life sciences ☐ Behavioural & social sciences ☐ Ecological, evolutionary & environmental sciences

For a reference copy of the document with all sections, see nature.com/documents/nr-reporting-summary-flat.pdf

Life sciences study design

All studies must disclose on these points even when the disclosure is negative.

Sample size	No statistical methods were used to calculate the sample size of the IMPACT cohort. Sample size was determined based on the number of patients admitted to Yale-New Haven Hospital (YNHH) between March 18th and May 18th that were enrolled and consented with th current study. This study enrolled 185 patients admitted to the Yale New Haven Health care network and 63 healthcare workers. Patients were identified though screening of EMR records for potential enrollment. Informed consent was obtained by trained staff and sample collection commenced immediately upon study enrollment. Clinical specimens were collected approximately every 4 days where an individual's clinical status permitted, and was continued until patient discharge or expiration. For mouse experiments, autoantibody functional assays, and autoantibody ELISA validations, the sample size was determined empirically based on prior studies and literatures of the field with similar experimental paradigms to provide sufficient statistical power for the assessment of biological effects of interests. No statistical methods were utilized to predetermine the sample size.
Data exclusions	Patients and samples were excluded from subsequent analysis if, during EMR review, they were found to be on active chemotherapy for unrelated malignancy, had any metastatic disease burden, were solid organ transplant recipients, or received convalescent COVID-19 serum as part of clinical trail not affiliated with the current work.
Replication	All experiments not involving mice were performed with technical replicates. All mouse experiments were repeated at least two times. Typically 5 mice were used per group per experiment. Experimental repeats showed similar trends and led to same conclusions. All data presented in the figures were pooled from at least two independent experiments.
Randomization	Randomization is not relevant to the research performed on human samples since those studies were observational in nature. Patients were stratified by disease severity (mild, moderate, and severe) based on based on oxygen levels and intensive care unit (ICU) requirement. Mild disease status (Clinical Score 0) was defined as SARS-CoV-2 infection not requiring hospitalization as a result of COVID-19 symptoms. Moderate disease status (Clinical Score 1, 2 and 3) was defined as: (1) SARS-CoV-2 infection requiring hospitalization without supplemental oxygen, (2) infection requiring non-invasive supplemental oxygen (<3 L / min, sufficient to maintain greater than 92% SpO2), (3) infection requiring non-invasive supplemental oxygen (> 3L supplemental oxygen to maintain SpO2 > 92%, or, required > 2L supplemental oxygen to maintain SpO2 > 92% and had a high sensitivity C-reactive protein (CRP) > 70) and received tocilizumab. Severe disease status (Clinical score 4 and 5) was defined as infection meeting all criteria for clinical score 3 while also requiring admission to the YNHH Intensive Care Unit (ICU) and > 6L supplemental oxygen to maintain SpO2 > 92% (4); or infection requiring invasive mechanical ventilation / extracorporeal membrane oxygenation (ECMO) in addition to glucocorticoid / vasopressor administration (5). Clinical score 6 was assigned for deceased patients. For mouse experiments, all mice were assigned randomly to experimental and control groups. For mouse experiments, age- and sex-matched mice were randomly assigned to experimental groups at the beginning of in vivo experiments. For autoantibody functional assays and autoantibody ELISA validations, randomization was not relevant because the experiments involved comparing samples from predetermined groups based on autoantibody positivity in our REAP screen. Control of other covariates was not relevant because autoantibody positivity was the only stratifying factor we were interested in comparing.
Blinding	At the time of sample acquisition and processing, scientists were completely unaware of the patients' conditions. Blood acquisition is performed and recorded by a separate team. Information on patients' conditions were not available until after processing and analyzing raw flow cytometry and REAP data. A clinical team, separate from the experimental team, performs chart review to determine patients' relevant statistics. Patients clinical information and clinical scores coding were only revealed after data collection. For mouse experiments, autoantibody functional assays, autoantibody ELISA validations, and anti-SARS-CoV-2 antibody ELISAs, investigators were not blinded as there was no subjective measurement.

Reporting for specific materials, systems and methods

We require information from authors about some types of materials, experimental systems and methods used in many studies. Here, indicate whether each material, system or method listed is relevant to your study. If you are not sure if a list item applies to your research, read the appropriate section before selecting a response.

Materials & experimental systems

n/a	Involved in the study
☐	☒ Antibodies
☐	☒ Eukaryotic cell lines
☒	☐ Palaeontology and archaeology
☐	☒ Animals and other organisms
☐	☒ Human research participants
☒	☐ Clinical data
☒	☐ Dual use research of concern

Methods

n/a	Involved in the study
☒	☐ ChIP-seq
☐	☒ Flow cytometry
☒	☐ MRI-based neuroimaging

Antibodies

Antibodies used

For each anti-human antibody, clone number, dilution, vendor, and catalogue number are listed below: BB515 anti-hHLA-DR (G46-6, 1:400, BD Biosciences, 564516), BV785 anti-hCD16 (3G8, 1:100, BioLegend, 302046), PE-Cy7 anti-hCD14 (HCD14, 1:300, BioLegend, 325618), BV605 anti-hCD3 (UCHT1, 1:300, BioLegend, 300460), BV711 anti-hCD19 (SJ25C1, 1:300, BD Biosciences, 563038), AlexaFluor 647 anti-hCD1c (L161, 1:150, BioLegend, 331510), Biotin anti-hCD141 (M80, 1:150, BioLegend, 344108), PE-Dazzle594 anti-hCD56 (HCD56, 1:300, BioLegend, 318348), PE anti-hCD304 (12C2, 1:300, BioLegend, 354504), APCFire750 anti-hCD11b (ICRF44, 1:100, BioLegend, 301352), PerCP/Cy5.5 anti-hCD66b (G10F5, 1:200, BD Biosciences, 562254), BV785 anti-hCD4 (SK3, 1:200, BioLegend, 344642), APCFire750/PE-Cy7/BV711 anti-hCD8 (SK1, 1:200, BioLegend, 344746/344712/344734), BV421 anti-hCCR7 (G043H7, 1:50, BioLegend, 353208), AlexaFluor 700 anti-hCD45RA (HI100, 1:200, BD Biosciences, 560673), PE anti-hPD1 (EH12.2H7, 1:200, BioLegend, 329906), APC anti-hTIM3 (F38-2E2, 1:50, BioLegend, 345012), BV711 anti-hCD38 (HIT2, 1:200, BioLegend, 303528), BB700 anti-hCXCR5 (RF8B2, 1:50, BD Biosciences, 566470), PE-Cy7/BV711 anti-hCD127 (HIL-7R-M21, 1:50, BD Biosciences, 560822/ 563165), PE-CF594 anti-hCD25 (M-A251, 1:200, BD Biosciences, 562403), BV785 anti-hCD19 (SJ25C1, 1:300, BioLegend, 363028), BV421 anti-hCD138 (MI15, 1:300, BioLegend, 356516), AlexaFluor700 anti-hCD20 (2H7, 1:200, BioLegend, 302322), AlexaFluor 647 anti-hCD27 (M-T271, 1:350, BioLegend, 356434), PE/Dazzle594 anti-hIgD (IA6-2, 1:400, BioLegend, 348240), PE-Cy7 anti-hCD86 (IT2.2, 1:100, BioLegend, 305422), APC/Fire750 anti-hIgM (MHM-88, 1:250, BioLegend, 314546), BV605 anti-hCD24 (ML5, 1:200, BioLegend, 311124), BV421 anti-hCD10 (HI10a, 1:200, BioLegend, 312218), BV421 anti-hCD15 (SSEA-1, 1:200, BioLegend, 323040), AlexaFluor 700 Streptavidin (1:300, ThermoFisher, S21383), BV605 Streptavidin (1:300, BioLegend, 405229), anti-STAT5 pY694 (47/Stat5, 1:50, BD Biosciences, 562077), anti-STAT1 pY701 (4a, 1:50, BD Biosciences, 612564), purified anti-CD3ε (OKT3, 1:100, BioLegend, 317301), anti-CD38 (MAB2404, 1:100, R&D systems, MAB2404-100), and Biotin anti-IgG Fc (HP6017, 1:100, BioLegend, 409308).

For each anti-mouse antibody, clone number, dilution, vendor, and catalogue number are listed: FITC anti-mCD11c (N418, 1:400, BioLegend, 117306), PerCP-Cy5.5/FITC anti-mLy6C (HK1.4, 1:400, BioLegend, 128012/128006), PE/BV605/BV711 anti-mNK1.1 (PK136, 1:400, BioLegend, 108708/108740/108745), PE-Cy7 anti-mB220 (RA3-6B2, 1:200, BioLegend, 103222), APC anti-mXCR1 (ZET, 1:200, BioLegend, 148206), APC/AlexaFluor 700/APC-Cy7 anti-mCD4 (RM4-5, 1:400, BioLegend, 100516/100536/100526), APC-Cy7 anti-mLy6G (1A8, 1:400, BioLegend, 127624), BV605/ Pacific Blue anti-mCD45 (30-F11, 1:400, BioLegend, 103140/103126), BV711/ PerCP-Cy5.5 anti-mCD8a (53-6.7, 1:400, BioLegend, 100748/100734), AlexaFluor 700/BV785 anti-mCD11b (M1/70, 1:400, BioLegend, 101222/101243), PE anti-mCXCR3 (CXCR3-173, 1:200, BioLegend, 126506), PE-Cy7 anti-mTCRgd (GL3, 1:200, BioLegend, 118124), AlexaFluor 647 anti-mCD19 (6D5, 1:200, BioLegend, 115522), AlexaFluor 700/BV711 anti-mCD44 (IM7, 1:200, BioLegend, 103026/103057), Pacific Blue anti-mCD69 (H1.2F3, 1:100, BioLegend, 104524), BV605/APC-Cy7 anti-mCD3 (17A2, 1:200, BioLegend, 100237/100222), BV605/APC-Cy7 anti-mTCRb (H57-597, 1:200, BioLegend, 109241/109220), BV785 anti-mCD45.2 (104, 1:400, BioLegend, 109839), FITC anti-mKLRG1 (2F1/KLRG1, 1:200, BioLegend, 138410), PE anti-mCD27 (LG.3A10, 1:200, BioLegend, 124210), Pacific Blue anti-I-A/I-E (M5/114.15.2, 1:400, BioLegend, 107602).

Validation

All antibodies used in this study are commercially available, and all have been validated by the manufacturers and used by other publications. Likewise, we titrated these antibodies according to our own our staining conditions. Further information can be obtained from vendors' websites.

The following anti-human antibodies were validated in the indicated species and applications: BB515 anti-hHLA-DR (G46-6) (BD Biosciences) (Human, Rhesus, Cynomolgus, Baboon, Dog) (FC), BV785 anti-hCD16 (3G8) (BioLegend) (Human, African Green, Baboon, Capuchin Monkey, Chimpanzee, Cynomolgus, Marmoset, Pigtailed Macaque, Rhesus, Sooty Mangabey, Squirrel Monkey) (FC, CyTOF), PE-Cy7 anti-hCD14 (HCD14) (BioLegend) (Human) (FC), BV605 anti-hCD3 (UCHT1) (BioLegend) (Human, Chimpanzee) (FC), BV711 anti-hCD19 (SJ25C1) (BD Biosciences) (Human) (FC), AlexaFluor647 anti-hCD1c (L161) (BioLegend) (Human, African Green, Baboon, Cynomolgus, Rhesus) (FC), Biotin anti-hCD141 (M80) (BioLegend) (Human, African Green, Baboon) (FC), PE-Dazzle594 anti-hCD56 (HCD56) (BioLegend) (Human, African Green, Baboon, Cynomolgus, Rhesus) (FC), PE anti-hCD304 (12C2) (BioLegend) (Human) (FC), APCFire750 anti-hCD11b (ICRF44) (BioLegend) (Human, African Green, Baboon, Chimpanzee, Common Marmoset, Cynomolgus, Rhesus, Swine) (FC), PerCP/Cy5.5 anti-hCD66b (G10F5) (BD Biosciences) (Human) (FC), BV785 anti-hCD4 (SK3) (BioLegend) (Human) (FC), APCFire750/PE-Cy7/BV711 anti-hCD8 (SK1) (BioLegend) (Human, Cross-Reactivity: African Green, Chimpanzee, Cynomolgus, Pigtailed Macaque, Rhesus, Sooty Mangabey) (FC), BV421 anti-hCCR7 (G043H7) (BioLegend) (Human, African Green, Baboon, Cynomolgus, Rhesus) (FC), AlexaFluor 700 anti-hCD45RA (HI100) (BD Biosciences) (Human) (FC), PE anti-hPD1 (EH12.2H7) (BioLegend) (Human, African Green, Baboon, Chimpanzee, Common Marmoset, Cynomolgus, Rhesus, Squirrel Monkey) (FC), APC anti-hTIM3 (F38-2E2) (BioLegend) (Human) (FC), BV711 anti-hCD38 (HIT2) (BioLegend) (Human, Chimpanzee, Horse) (FC), BB700 anti-hCXCR5 (RF8B2) (BD Biosciences) (Human) (FC), PE-Cy7/BV711 anti-hCD127 (HIL-7R-M21) (BD Biosciences) (Human) (FC), PE-CF594 anti-hCD25 (BC96) (BD Biosciences) (Human, Rhesus, Cynomolgus, Baboon) (FC), BV785 anti-hCD19 (SJ25C1) (BioLegend) (Human) (FC), BV421 anti-hCD138 (MI15) (BioLegend) (Human) (FC), AlexaFluor700 anti-hCD20 (2H7) (BioLegend) (Human, Baboon, Capuchin Monkey, Chimpanzee, Cynomolgus, Pigtailed Macaque, Rhesus, Squirrel Monkey) (FC), AlexaFluor 647 anti-hCD27 (M-T271) (BioLegend) (Human, Cross-Reacitivity: Baboon, Cynomolgus, Rhesus) (FC), PE/Dazzle594 anti-hIgD (IA6-2) (BioLegend) (Human) (FC), PE-Cy7 anti-hCD86 (IT2.2) (BioLegend) (Human, African Green, Baboon, Capuchin Monkey, Common Marmoset,

Cotton-topped Tamarin, Chimpanzee, Cynomolgus, Rhesus) (FC), APC/Fire750 anti-hIgM (MHM-88) (BioLegend) (Human, African Green, Baboon, Cynomolgus, Rhesus) (FC), BV605 anti-hCD24 (ML5) (BioLegend) (Human, Cross-Reactivity: Chimpanzee) (FC), BV421 anti-hCD10 (HI10a) (BioLegend) (Human, African Green, Baboon, Capuchin monkey, Chimpanzee, Cynomolgus, Rhesus) (FC), BV421 anti-hCD15 (SSEA-1) (BioLegend) (Human) (FC), AlexaFluor 700 Streptavidin (1:300) (ThermoFisher) (FC), BV605 Streptavidin (1:300) (BioLegend) (FC), PE anti-STAT5 pY694 (1:50) (BD Biosciences) (Human) (FC), anti-STAT1 pY701 (4a) (BD Biosciences) (Human, Mouse) (FC), purified anti-CD3ε (OKT3) (BioLegend) (Human) (FC), anti-CD38 (MAB2404) (R&D systems) (Human) (FC, CyTOF, IP, ICC), and Biotin anti-IgG Fc (HP6017) (BioLegend) (Human) (FC).

The following anti-mouse antibodies were validated in the indicated species and applications: FITC anti-mCD11c (N418) (BioLegend) (Mouse) (FC), PerCP-Cy5.5/FITC anti-mLy6C (HK1.4) (BioLegend) (Mouse) (FC), PE or BV605 or BV711 anti-mNK1.1 (PK136) (BioLegend) (Mouse) (FC), PE-Cy7 anti-mB220 (RA3-6B2) (BioLegend) (Mouse, Human, Cat) (FC), APC anti-mXCR1 (ZET) (BioLegend) (Mouse, Rat) (FC), APC or AlexaFluor 700 or APC-Cy7 anti-mCD4 (RM4-5) (BioLegend) (Mouse) (FC), APC-Cy7 anti-mLy6G (1A8) (BioLegend) (Mouse) (FC), BV605/Pacific Blue anti-mCD45 (30-F11) (BioLegend) (Mouse) (FC), BV711 or PerCP-Cy5.5 anti-mCD8a (53-6.7) (BioLegend) (Mouse) (FC), AlexaFluor 700 or BV785 anti-mCD11b (M1/70) (BioLegend) (Mouse, Human, Chimpanzee, Baboon, Cynomolgus, Rhesus, Rabbit) (FC), PE anti-mCXCR3 (CXCR3-173) (BioLegend) (Mouse) (FC), PE-Cy7 anti-mTCRgd (GL3) (BioLegend) (Mouse) (FC), AlexaFluor 647 anti-mCD19 (6D5) (BioLegend) (Mouse) (FC, IHC-F), AlexaFluor 700 or BV711 anti-mCD44 (IM7) (BioLegend) (Mouse, Human, Baboon, Chimpanzee, Cynomolgus, Rhesus, Squirrel Monkey, Horse, Cattle, Swine, Dog, Cat) (FC), Pacific Blue anti-mCD69 (H1.2F3) (BioLegend) (Mouse) (FC), BV605 or APC-Cy7 anti-mCD3 (17A2) (BioLegend) (Mouse) (FC), BV605 or APC-Cy7 anti-mTCRb (H57-597) (BioLegend) (Mouse) (FC), BV785 anti-mCD45.2 (104) (BioLegend) (Mouse) (FC), FITC anti-mKLRG1 (2F1/KLRG1) (BioLegend) (Mouse, Human) (FC), PE anti-mCD27 (LG.3A10) (BioLegend) (Mouse, Rat, Human) (FC), Pacific Blue anti-I-A/I-E (M5/114.15.2) (BioLegend) (Mouse) (FC).

Eukaryotic cell lines

Policy information about cell lines

Cell line source(s)	TF-1 (ATCC, CRL-2003), Expi293F cells (Thermo Fisher Scientific, A14527), Sf9 cells (Expression Systems, 94-001F), Hi-5 cells (Expression Systems), Jurkat cells (ATCC, TIB-152), Raji cells (ATCC, CCL-86), THP-1 cells (ATCC, TIB-202), L-929 cells (ATCC, CCL-1). HTLA cells were a kind gift from Noah Palm and were originally derived by Barnea et al., 2008 (doi: 10.1073/pnas.0710487105)
Authentication	The TF-1, Expi293F, Sf9, Hi-5, Jurkat, Raji, THP-1, and L-929 cell lines were purchased commercially and not authenticated by us. The HTLA cell line was previously reported but not authenticated by us.
Mycoplasma contamination	No cell lines were tested for mycoplasma contamination.
Commonly misidentified lines (See ICLAC register)	none

Animals and other organisms

Policy information about studies involving animals; ARRIVE guidelines recommended for reporting animal research

Laboratory animals	For SARS-CoV-2 infection, K18-hACE2 mice (Stock #: 034860) were purchased from the Jackson Laboratory. For bone marrow stem cell isolation, C57BL/6 mice (Stock #: 000664) were purchased from the Jackson Laboratory. Six- to ten-week-old male and female mice were used throughout the experiment. For bone marrow stem cell isolation, Bone marrow stem cells were isolated from eight-week-old mice. All mice were housed as groups of 5 to 6 individuals per cage and maintained on a 12-hour light/dark cycle (lights on at 7:00 AM) at 22–25°C temperature and 30–70% relative humidity under specific-pathogen free conditions. All mice were fed with regular rodent's chow and sterilized water ad libitum.
Wild animals	No wild animals were used.
Field-collected samples	No field-collected samples were used.
Ethics oversight	All procedures used in this study complied with federal guidelines and the institutional policies of the Yale School of Medicine Animal Care and Use Committee.

Note that full information on the approval of the study protocol must also be provided in the manuscript.

Human research participants

Policy information about studies involving human research participants

Population characteristics	Demographic information is included in Extended Data Table 1.
Recruitment	Patients admitted to the Yale New Haven Hospital (YNHH) between March 18th and May 18th, were recruited to the Yale IMPACT study (Implementing Medical and Public Health Action Against Coronavirus CT) after testing positive for SARS-CoV2 by qRT-PCR. (serology was further confirmed for all patients enrolled). Patients were identified though screening of EMR records for potential enrollment with no self selection. Informed consent was obtained by trained staff and sample collection commenced immediately upon study enrollment. Clinical specimens were collected approximately every 4 days where an individual's clinical status permitted, and was continued until patient discharge or expiration. Potential study biases include

	the enrollment of only hospitalized COVID-19 patients for subsequent analysis, and recruitment of only healthcare workers as heatlhy, uninfected negative control samples.
Ethics oversight	Yale Human Research Protection Program Institutional Review Boards. Informed consents were obtained from all enrolled patients and healthcare workers. Our research protocol was reviewed and approved by the Yale School of Medicine IRB and HIC (#2000027690). Informed consent was obtained by trained staff and records maintained in our research database for the duration of our study. There were no minors included on this study.

Note that full information on the approval of the study protocol must also be provided in the manuscript.

Flow Cytometry

Plots

Confirm that:

☒ The axis labels state the marker and fluorochrome used (e.g. CD4-FITC).

☒ The axis scales are clearly visible. Include numbers along axes only for bottom left plot of group (a 'group' is an analysis of identical markers).

☒ All plots are contour plots with outliers or pseudocolor plots.

☒ A numerical value for number of cells or percentage (with statistics) is provided.

Methodology

Sample preparation	For human studies, freshly isolated PBMCs were stained for live and dead markers for 30 min at 4 °C, blocked with Human TruStan FcX for 30 min at 4 °C, stained for surface markers for 30 min at 4 °C and then fixed with with 4% formaldehyde for 45 min at 4 °C before being acquired on Attune NXT. For mouse studies, lung tissues were collected at the experimental end point, digested with collagenase A and DNase I in complete RPMI-1640 media for 30 min at 37 °C, and mechanically minced. Lung samples were filtered to single cell suspension and further treated with ACK buffer to remove red blood cells. Single cell suspension was then blocked with anti-mouse CD16/32 antibodies for 30 min at 4 °C and stained with surface antibodies for 30 at 4 °C. Dead cells were excluded with Fixable Aqua added together with anti-CD16/32. Cells were fixed with 4% formaldehyde for 45 min at 4 °C before being acquired on Attune NXT. For macrophage antibody dependent cellular phagocytosis assays, to isolate bone marrow stem cells, femurs and tibias from 8-week old C57BL/6 mice (housed as described above and in the Methods) were dissected and flushed with complete RPMI-1640 media. Cells were resuspended in RPMI (+ 10% heat inactivated FBS, 10 U/mL Penicillin, 100 mg/mL Streptomycin; cRPMI) with 30% (vol/vol) L929 fibroblast conditioned media as a source of M-CSF and incubated at 37 °C, 5% CO2. On day 3 post-isolation, 10 mL L929 fibroblast conditioned media was added to plates. 200,000 BMDMs (7 days post isolation) were plated on non-TC treated 6-well plates in cRPMI + 10% L929 media. The following day, BMDMs were incubated with appropriate serum/IgG for 30 minutes on ice and Raji/Jurkat cells for 3 hours at 37 °C, 5% CO2. Raji (ATCC, CCL-86) or Jurkat (ATCC, TIB-152) cells were labelled using CellTrace Far Red (Thermo Fisher) according to standard manufacturer protocols. BMDMs were detached from the plate after a 3-hour incubation using 10 mM EDTA PBS and stained with anti-mouse CD45 – Pacific blue (clone 30-F11, BioLegend) for 30 minutes at 4 °C before being acquired on a CytoFLEX flow cytometer. For anti-GM-CSF and anti-IFN-I functional assay, TF-1 cells (ATCC, CRL-2003) or THP-1 cells (ATCC, TIB-202) were used respectively. TF-1 cells were cultured in RPMI (+ 10% heat inactivated FBS, 10 U/mL Penicillin, 100 mg/mL Streptomycin, 1 mM sodium pyruvate, 2 ng/mL GM-CSF (PeproTech, 300-03)) and incubated at 37 °C, 5% CO2. THP-1 cells were cultured in RPMI (+ 10% heat inactivated FBS, 10 U/mL Penicillin, 100 mg/mL Streptomycin) and incubated at 37 °C, 5% CO2. TF-1 or THP-1 cells were stimulated and then fixed in 4% paraformaldehyde for 30 mins, washed with PBS, and permeabilized in 100% methanol on ice for 45 minutes. Cells were then washed twice with PBE and stained with PE conjugated anti-STAT5 pY694 (1:50) (BD Biosciences, 562077) or anti-STAT1 pY701 (1:50) (BD Biosciences, 612564) and human TruStain FcX (1:100) (BioLegend, 422302) for 1 hour at room temperature. Cells were washed with PBE and acquired on a SA3800 flow cytometer.
Instrument	Cells were acquired on an Attune NXT (ThermoFisher), SA3800 flow cytometer (Sony), or CytoFLEX flow cytometer (Beckman Coulter).
Software	Data were analysed using FlowJo software version 10.6 software (Tree Star).
Cell population abundance	Cell sorting was not performed in this study.
Gating strategy	For all experiments, FSC-A/SSC-A gates of the starting cell population were used to identify lymphocytes. FSC-A/FSC-H gates if lymphocytes were used to identify singlets. Additional gates to identify various immune cell subsets are available in Extended Data Figure 4h,i, Extended Data Figure 6e,g,h, and Extended Data Figure 8.

☒ Tick this box to confirm that a figure exemplifying the gating strategy is provided in the Supplementary Information.